AIAA AVIATION Forum
June 27-July 1, 2022, Chicago, IL & Virtual
AIAA AVIATION 2022 Forum

10.2514/6.2022-3255

# Development of a Simulation Environment to Track Key Metrics to Support Trajectory Energy Management of Electric Aircraft

Johannes A. Verberne*, Seumas M. Beedie †, Caleb M. Harris‡, Cedric Y. Justin§ and Dimitri N. Mavris¶
*Aerospace Systems Design Laboratory, School of Aerospace Engineering*
*Georgia Institute of Technology, Atlanta, GA, 30332, USA*

**Growing concerns worldwide about anthropogenic climate change are leading to significant research in ways to reduce greenhouse gas emissions. Technologies are investigated to improve the overall energy efficiency of flying vehicles, and among these, new powertrain technologies less reliant on fossil fuels are especially promising. Concurrently, the expected growth of new market segments, such as urban air mobility and regional air mobility where vehicles are envisioned to operate over densely populated areas, will lead to increased scrutinity regarding the vehicle emissions and the vehicle safety. In this context, significant research has been carried out in the field of electric and hybrid-electric aircraft propulsion. Driven by significant strides made by the automotive industry regarding electric battery technology, the aspirational goal of *useful* electric flight is now within reach. Significant challenges nonetheless remain regarding the certification of these new vehicles to ensure an equivalent level of safety. Indeed, the behavior of electric powertrains is more complex than that of traditional powertrains and features additional thermal and ageing constraints that need to be contended with. Moreover, the ability of many of these vehicles to fly both on their wing or on their rotors brings another level of sophistication that will increase the workload of flight crews. Combined, these might adversely impact the safety of flight. This research aims to elucidate some of these challenges by providing insights into the behavior and idiosyncracies of new electrified vehicles and by identifying visual cues that should be provided to flight crews to support safe decision-making in the cockpit. Besides these visual cues, we explore functionalities that a Trajectory Energy Management system could feature to improve flight safety by providing insights into the management of stored usable energy and by monitoring critical parameters of electrified powertrains. This paper includes two use-cases in which the functionality of the Trajectory Energy Management system is explored for pre-flight planning and in-flight diversion decision-making applications.**

## I. Nomenclature

| | | |
|---|---|---|
| 3DOF | = | 3 Degrees of Freedom |
| 6DoF | = | 6 Degrees of Freedom |
| AAM | = | Advanced Air Mobility |
| AO-RRT | = | Asymptotically-Optimal Rapidly Exploring Random Tree |
| CFR | = | Code of Federal Regulations |
| CTOL | = | Conventional Take-Off and Landing |
| EASA | = | European Union Aviation Safety Agency |
| ECM | = | Equivalent Circuit Module |
| EPU | = | Electric Propulsion Unit |
| eVTOL | = | Electric Vertical Take-off and Landing |
| GA | = | General Aviation |
| KMHV | = | Mojave Air and Space Port |

*Graduate Research Associate, School of Aerospace Engineering
†Graduate Research Associate, School of Aerospace Engineering
‡Graduate Research Associate, School of Aerospace Engineering
§Research Engineer II, School of Aerospace Engineering, AIAA Member
¶S.P. Langley Distinguished Regents Professor and Director of ASDL, AIAA Fellow

KRAL = Riverside Municipal Airport
KSNA = Orange County Airport
L71 = California City Municipal Airport
IFR = Instrument Flight Rules
MCP = Maximum Continuous Power
MTOP = Maximum Take-off Power
MTOW = Maximum Take-Off Weight
NASA = National Aeronautics and Space Administration
NDARC = NASA Revolutionary Vertical Lift Technology
OAT = Outside Air Temperature
RRT = Rapidly Exploring Random Tree
RVLT = Revolutionary Vertical Lift Technology
SOC = State of Charge
SOH = State of Health
SRTM = Shuttle Radar Topography Mission
SST = Stable Sparse RRT
SST* = Asymptotically Optimal SST
TEM = Trajectory Energy Management
UAM = Urban Air Mobility
VFR = Visual Flight Rules
VTOL = Vertical Take-off and Landing

## II. Introduction

The past decades have seen both a steady increase in the global population and an overall migration into cities. This increase in population in the vicinity of large cities will most certainly lead to more vehicles, more congestion, and more traffic-related delays. In this context, novel urban and regional air mobility operations have been envisioned to bypass traffic and provide quick and efficient transportation within metropolitan areas and their immediate surroundings. At the same time, the planet as a whole is facing a possible climate emergency that calls for demanding carbon emissions mitigation policies. These challenges, together with general improvements in battery technology, have led to a recent paradigm shift in aviation towards electric and hybrid-electric aircraft, particularly for urban, suburban, and regional air mobility operations. This novel niche of Advanced Air Mobility (AAM) vehicles provides the first step towards electrifying aviation. AAM vehicles promise a smaller environmental footprint due to their hybrid-electric or electric drivetrains and their Vertical Take-Off and Landing (VTOL) capabilities. However, the novelty of these powertrains and overall vehicle configuration means that much is still unknown regarding their operations compared to the well-established reciprocating and turboshaft-driven vehicles. Further research is therefore required to understand key differences between conventional fossil-fuel burning powertrains and electric powertrains before civil aviation regulators can pencil policies, regulations, and means of compliance to ensure an equivalent level of safety. The proposed Trajectory Energy Management (TEM) system offers a solution to investigate the behavior of key powertrain metrics over the course of simulated missions.

Trajectory Energy Management (TEM) deals with the management of energy and the overall monitoring of the powertrain during a specified vehicle mission. For conventional reciprocating drivetrain vehicles, the energy expenditure during a mission is well understood [1]. For electric powertrain vehicles, the overall energy available and energy consumption are less trivial to assess, and new metrics never used before may be required to accurately depict the *energy state*. In a previous study, a modeling framework was presented to identify and analyze some of these key metrics required to support the TEM of electric aircraft [2]. As this study discussed, the modeling of a fully-electric drivetrain provides some challenges related to nonlinear battery performance, thermal management requirements, and limited specific energy density of current battery technology. Furthermore, these challenges provided the motivation to support the development of a modeling framework that would allow for the identification of key metrics most pertinent to the overall TEM system of an electric aircraft. These key metrics enable accurate and unambiguous predictions of the usable energy remaining on board, as well as the remaining range and endurance of the vehicle.

This paper is a continuation of the research presented in [2] towards developing a full TEM modeling and simulation capability for electric aircraft. Whereas [2] focused on presenting the initial capability to allow for the simulation of the evolution of key powertrain metrics during a fixed-wing vehicle mission, the present research focuses on new capabilities

developed for VTOL-capable aircraft. In addition, significant improvements to the overall powertrain modeling and trajectory generation capabilities are highlighted. The research presented in this paper highlights in greater detail some of the underpinning assumptions of the vehicle, powertrain, and trajectory-generation models used in a sister-paper presented at the AIAA Aviation 2022 Conference [3].

This paper is organized as follows: Section III provides a literature review about the various topics of interest while Section IV describes in detail the overall modeling framework of the TEM system for the vehicle simulation and validation, the mission energy and power requirements, the electrified powertrain modeling, and the flight dynamics and powertrain-informed trajectory generation. Section V shows results of the TEM system simulation for two potential real-world scenarios for pre-flight planning and in-flight diversion decision-making while Section VI concludes the paper.

## III. Background

Traditional fossil fuel burning aircraft revolve around the traditional tube-and-wing family of aircraft or the traditional main-and-tail rotor family of helicopters where only minor configuration derivatives are considered. And yet, many new exotic configurations capable of VTOL operations are currently being pursued by the AAM community due to the need to operate in constrained urban environments where the ground footprint of operations comes at a premium and where tight maneuvering may be required. The electric Vertical Takeoff and Landing (eVTOL) Aircraft Directory maintained by the Vertical Flight Society shows a categorization of around 650 configurations including vectored thrust, lift+cruise, multicopter, and rotorcraft [4].

Of particular interest are the lift+cruise configurations which give the flight crew the possibility to either fly the aircraft as a traditional fixed-wing vehicle or as a rotorcraft. The presence of small wings on these configurations can be beneficial in loss of power emergency situations. Additionally, a lift+cruise configuration is typically more energy efficient for longer range missions due to a more efficient wing as compared to vehicles producing lift by vertical rotors [5]. This is beneficial given that one of the current main short comings of fully-electric aircraft is their range and endurance. Perhaps the most notable two examples of this configuration are the BETA Technologies ALIA of which 150 vehicles have been purchased in 2021 by the United Parcel Service (UPS) to perform time-sensitive cargo operations [6], and the Wisk Aero Cora which has recently been acquired by Boeing and is used by NASA's Advanced Air Mobility National Campaign to develop operations guidelines [7].

Due to the relative novelty of these new eVTOL configurations and owing to the drive of these companies to bring their designs to the market first, limited design and performance information is available in the public domain. A wealth of knowledge about the performance, aerodynamics and operation of some of these novel concept vehicles was however obtained through NASA's Revolutionary Vertical Lift Technologies (RVLT) program focusing on Urban Air Mobility (UAM) applications [8][9][10]. This study focused on highlighting the main differences between the quadrotor, side-by-side helicopter and lift+cruise configurations.

As mentioned, one operation difficulty with these fully-electric vehicles is their limited range and endurance as compared to their reciprocating counterparts [11]. Important therefore for these type of vehicles is the concept of Trajectory Energy Management (TEM) which concerns itself with the overall management and monitoring of the onboard energy and powertrain. To produce accurate results and predictions from the TEM system for a given aircraft, accurate models of the aircraft dynamics and powertrain are required both of which were discussed in the previous study for a notional fixed-wing aircraft based on the Pipistrel Velis Electro aircraft [2]. This flexible powertrain modeling framework is reused to represent the lift+cruise configuration investigated in this work. The modular nature of the framework allows for the additional vertical lift components to be modeled in parallel with the conventional (horizontal) powertrain. Appropriately scaled lift motors and inverters are defined in the framework, and contribute to the overall power and thermal load on the battery packs. The battery packs themselves are based on the previously validated equivalent circuit model (ECM) of a notional Pipistrel Velis Electro. This model was originally developed from the ECM methodology utilized by NASA to model the X-57 Maxwell experimental electric aircraft [12]. This model employs extensive characterization of 18650 LiPo cells used in the X-57 battery - the same type of cell comprising the Velis Electro battery - allowing the impact of temperature and State of Charge (SOC) on the battery to be modeled. The work of Falck et al [13] informed the development of a battery temperature model, allowing the simulated battery temperature and any associated constraints to be considered in the trajectory generation algorithm.

Using accurate models of the vehicle dynamics and its powertrain components, the TEM system can be leveraged to search and find optimum flight trajectories. For this research, the TEM system is extended to allow for the analysis of eVTOL-capable vehicles. This requires the computation of estimates of energy losses, the avoidance of collision with

terrain and other large obstacles, the modeling of flight dynamics that can handle a wide range of eVTOL designs, and the guarantee of flyability of the resulting trajectories. There exists literature examining trajectory planning for eVTOL or other complex dynamical models, but in this literature the trajectory planning is usually applied to other applications.

As discussed above, one considerable body of research on the topic of trajectory planning with model dynamics included was performed by NASA with their X-57 Maxwell flight demonstrator aircraft where the effects of powertrain component energy and thermal constraints were analyzed on different phases of flight which subsequently lead into the development of a multi-phase mission planning capability that can be used to simulate the aircraft and powertrain behavior of multiple aircraft trajectory phases [13][14]. Further previous works such as [15] require flight operation information including waypoints and flight performance data, and leverage a 3-DOF trajectory model that limits the fidelity of flight patterns and power estimates. Alternatively, in [16] an optimal control problem is defined and is modified to a convex optimization problem that can be solved quickly. The linearization reduces the accuracy of the solution and the hard constraints and optimization function must be setup for each different vehicle dynamics needed for analysis such as emergency landing or reachability analysis [17].

Trajectory generation itself has been performed in many ways, including optimization-based methods, grid-based methods, and sampling-based methods. While methods like optimal control are powerful, they require complex iterative solvers using collocation or shooting methods that are costly to compute in high-dimensions, or two-point boundary problem solutions using the Hamilton-Jacobi-Bellman or Pontryagin's Maximum Principle [18]. Grid-based methods are easy to define and develop since they require a single function to transition the vehicle from one grid cell to another, whether in 2D or 3D. However, these methods can be exhaustive and inaccurate depending on the choice of algorithm and transition function. Sampling-based methods leverage a stochastic technique and can guarantee completion and optimality with particular algorithms. Examples include probabilistic roadmaps [19] or Rapidly exploring Random Tree (RRT) [20]. RRT leverages efficient tree data structures, cost-based tree pruning, and random sampling for asymptotically optimal solutions and guaranteed completeness. In this application, trajectory generation must check for collisions with any terrain or known static obstacles if that data is available. Therefore, the methods mentioned before must include collision checks, in the form of constraints or geometric sampling. This can be performed using RRT derived trajectory generators.

Tree-based exploration has often been leveraged for solving high-dimensional search problems or for experimenting with complex edge functions with kinodynamic constraints. Advancements in tree-based exploration and kinodynamic planning have led to sparse-rapidly exploring random tree (sparse-RRT) [21] and asymptotically-optimal rapidly exploring random tree (AO-RRT) [22], which were demonstrated on a cart pendulum and a 2nd-order fixed-wing aircraft respectively. In [23] a kinodynamic planner with incremental sampling is developed for solving high-dimensional motion planning problems with asymptotic optimality while maintaining computational efficiency. This has been implemented for simulated eVTOL vehicles such as in [24].

As motivated in [2], a gap exists in the literature in the modeling and simulation capabilities of novel electric aircraft which can ultimately be leveraged into the TEM framework to perform in-flight energy management. This work seeks to enhance and extend the framework outlined in [2] for VTOL-capable vehicles.

## IV. Modeling Framework

The architecture of the TEM simulation environment is described in Figure 1 [2] which provides a blueprint of the simulation environment used to identify, analyze, and track key powertrain metrics of electric drivetrains over user-prescribed or autonomously-generated trajectories. The user provides the environment with vehicle characteristics together with mission objectives as an input to the simulation environment. At its core, the TEM system uses a trajectory generation and optimization capability using the mission objectives and vehicle definition in order to establish an energy-optimized and *flyable* trajectory. This flight trajectory is communicated to the energy analysis capability in the form of required shaft power at each point in the trajectory. The energy analysis capability then provides estimates about energy expenditures and any other relevant energy-metrics over the prescribed trajectory. This can be used to first facilitate the identification and understanding of critical energy-metrics that need to be provided to flight crew and then to support decision-making in the cockpit.

Previous research in [2] presented and discussed various parts of the TEM system in detail for fixed-wing vehicles. This research presents additional features and capabilities of the improved TEM system and particularly those pertinent to model VTOL-capable aircraft.

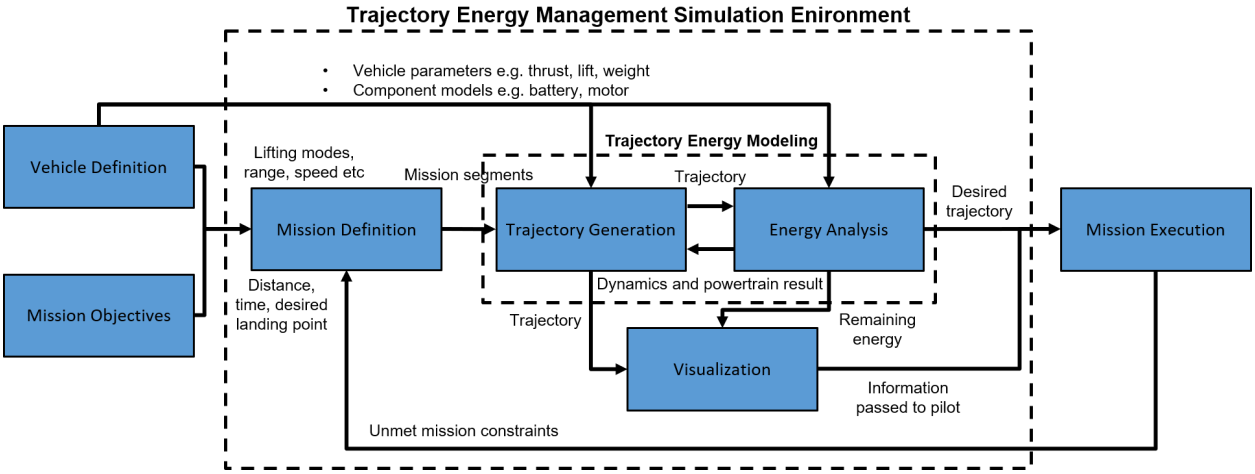


**Fig. 1 Architecture of the Trajectory Energy Management (TEM) Simulation Environment [2]**

### A. Vehicle Simulation Environment

Referring to Figure 1, a vehicle simulation is required for the 'Energy Analysis'-module to approximate and evaluate the power requirements during a specific mission. The power requirements for the mission can subsequently be fed to the powertrain module to analyze the health and charge of the battery together with power-related metrics utilizing a set of initial conditions. Beedie et al. [2] described the vehicle simulation of fixed-wing vehicles while this research focuses on the technical approach used to model the *lift-on-rotor* phases of flight of a generic VTOL mission. As described in [2], the simulation utilizes a dynamic model tracking a 12-state vector consisting of the body-axis velocities, Earth-axis positions, body-axis angular rates, and earth-axis Euler angles. The control vector consists of the typical elevator, aileron, and rudder deflections together with throttle settings. A trim algorithm modified from [25] is utilized to define the trimming of the vehicle in cruise, climb, descend and turn conditions as an optimization problem where dynamic constraints on velocities and accelerations provide the desired trimmed vehicle states and input vector. As will be discussed in greater detail in later sections, the trim routine for vertical flight is set up to solve for the required vertical thrust. Although assumed to be present, collective control of the vertical rotors is not explicitly modeled. As will be discussed, the key information of interest is the power demand in flight which can be obtained without the need of vertical rotor control modeling. A flight mission is built up by the concatenation of these individual trim segments where the transition between trim segments is assumed to be instantaneous.

#### *1. Notional Vehicle Models*

In order to show the workings of the TEM system in the modeling and simulation environment, a realistic use case is desired. In the previous research [2], a notional model of the Slovenian two-seater Pipistrel Velis Electro was presented. This is a fully-electric general aviation fixed-wing aircraft and also the first electric aircraft to obtain a type certificate from EASA in June 2020 (EASA.A.573 Type Certificate Data sheet) [26].

To demonstrate the TEM system capability for VTOL-capable aircraft, a *Lift+Cruise* vehicle inspired by one of the concepts generated under the NASA Revolutionary Vertical Lift Technology (RVLT) program is used [10]. This vehicle is described as the Lift+Cruise model in the literature [8]. This vehicle is chosen as a representative example of a future promising eVTOL UAM vehicle. At the same time, there is a relatively good amount of information about the aircraft and its characteristics in the public domain [8]. This vehicle concept was designed by NASA to explore UAM mission requirements and technology trades, and its effect on futuristic vehicle concepts with a 1,200 lb payload weight (up to six passengers). The NASA Design and Analysis of Rotorcraft (NDARC) tool [27], offering a rapid evaluation environment for requirements and technology trades in the vehicle design phase, was used to obtain a sized vehicle solution given a set of requirements.

The electric NASA RVLT Lift+Cruise vehicle utilizes eight vertical lifting electric motors rated at 141.2 kW maximum takeoff power for 150 seconds and 94.1 kW maximum continuous power both at 1050 RPM (Updated design originally based on [8]). These vertical motors drive eight 10 ft diameter propellers for vertical flight. One pusher electric motor is installed at the rear of the aircraft rated at 661.1 kW maximum takeoff power for 150 seconds and

440.7 kW maximum continuous power both at 1275 RPM. The pusher electric motor drives one six-blade 9 ft diameter propeller. These nine motors and all internal systems are powered by a 485 kWh, 2675.3 lb lithium-ion battery. Overall the electric NASA RVLT Lift+Cruise has a maximum takeoff weight (MTOW) of 9481.9 lb with a maximum payload weight of 1200 lb. Furthermore, the vehicle is equipped with a 57.72 ft wingspan wing with a total wing area of 274.8 $ft^2$.

As part of the NDARC tool, the internal sizing and synthesis capability uses a standardized design mission profile to evaluate the performance of the vehicle for a typical mission [28]. The specific mission utilized to evaluate the performance of the electric NASA RVLT Lift+Cruise vehicle can be seen in Figure 2. A 10 second timed hover at max power segment is performed at numbered locations 2 and 5 to simulate the transitioning of the vehicle from lift on rotors to lift on wing and vice-versa respectfully. Additionally, after the modeled transition at numbered location 5, an additional 30 second hover is commanded to account for any maneuvering near the landing site. A no-credit descend is performed at numbered location 4 which will occur at the moment the vehicle in cruise has reached the desired range of 37.5 nm measured from the starting location. A 20 minute reserve is added at the end of the mission at best range speed. Finally, the overall design mission is flown using a 10 kts headwind. The available design mission results from NDARC will be utilized to validate the developed vehicle model for the electric NASA RVLT Lift+Cruise vehicle in a later section.

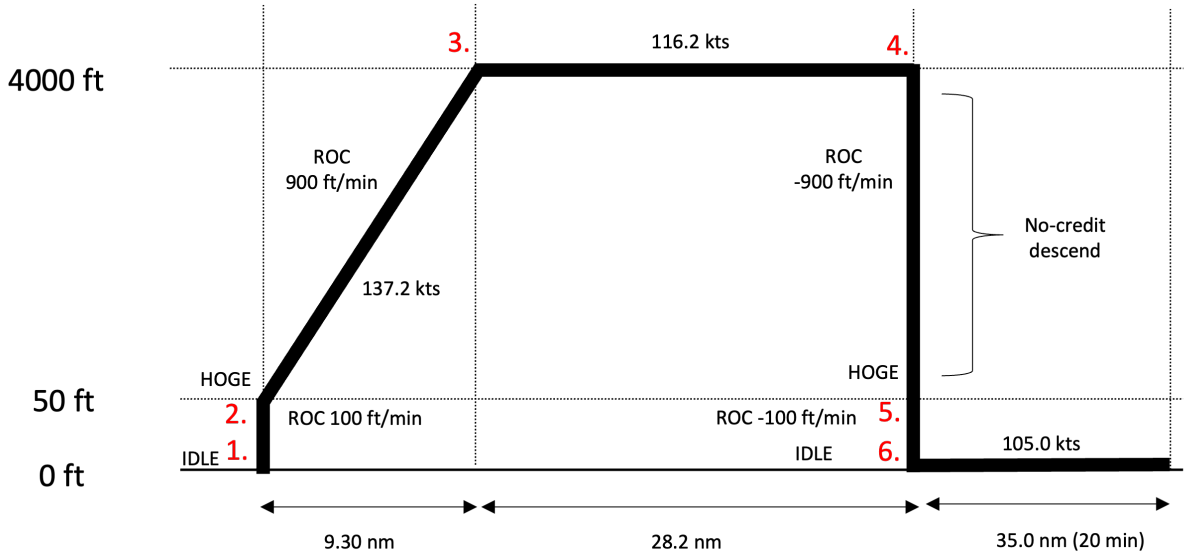


**Fig. 2 Electric NASA RVLT Lift+Cruise Design Mission**

*2. Helicopter Momentum Theory*

For a fixed-wing aircraft, an estimate for the overall power requirements at each operating point in the mission can be determined relatively straightforward using momentum theory by multiplying the thrust by the freestream velocity:

$$P = TV_{\infty} \tag{1}$$

In a similar fashion, momentum theory applying conservation laws of fluid mechanics can be utilized to determine the power requirements in vertical flight by analyzing the flow around and into a spinning rotor. In general, the total power required for vertical flight can be estimated by summing the individual contributions for induced, parasite, climb and profile powers (Equation 2) [29][30]. Induced power represents the power required to induce a downward momentum to the air flowing through a spinning vertical rotor to generated lift, parasite power represents the extra power required for forward flight, climb power represents the power required for potential energy increase, and finally the profile power represents extra power required to overcome the viscous drag of the spinning rotor.

$$P_{total} = P_{induced} + P_{parasite} + P_{climb} + P_{profile} \tag{2}$$

For vertical descend, hover and vertical climb the total power can be defined as shown in Equation 3 [29][30]:

$$P_{total} = TV_c + \kappa Tv + P_{profile} = TV_c + \kappa T\left(\frac{-V_c}{2} + \sqrt{\left(\frac{V_c}{2}\right)^2 + v_h^2}\right) + P_{profile} \tag{3}$$

where, $V_c$ is the vertical rate of climb/descend, $\kappa$ is an correction to account for additional losses and $v_h$ is the hover induced velocity defined as:

$$v_h = \sqrt{T/2\rho A} \tag{4}$$

where $\rho$ is the air density and A is the rotor disc area. Comparing Equation 2 and Equation 3, the first term in Equation 3 determines the climb power while the second term calculates the induced power of the vehicle at a certain flight condition. Since there is no forward flight component the parasite drag is zero.

In the case for forward flight, that is cruise, climb or descend, the required power can be calculated as [29][30]:

$$P_{total} = WV_c + DV_\infty + \kappa Tv + P_{profile} = TV_\infty \sin\alpha_{tpp} + \kappa Tv + P_{profile} \tag{5}$$

where, $\alpha_{tpp}$ is the local angle of attack at the rotor disc, W is the weight of the vehicle, D is the total drag force in forward flight and $v$ is the induced velocity defined as

$$v = \frac{v_h^2}{\sqrt{(V_\infty \cos(\alpha_{tpp}))^2 + (V_\infty \sin(\alpha_{tpp}) + v)^2}} \tag{6}$$

Again, comparing Equation 2 and Equation 5 shows that the first term in Equation 5 combines the parasite and climb power by utilization of a small angle approximation while the second term defines the induced power at the flight condition.

In general, the above equations hold for normal operation, small descend rates and very steep descend rates (windmill brake states). For moderate descend rates, that is for which the ratio $V/v_h$ is between -0.3 and -2, the rotor finds itself in a vortex ring state where the tip vortices by the spinning propeller cause turbulent interactions. In this state the above shown momentum theory equations do not hold and an empirical model is used to match power requirements based on flight test data [29].

As a validation step of the momentum theory in the simulation environment, a rotor power plot can be constructed in vertical and forward flight from the simulation environment and compared to its theoretical counterpart shown in [30]. This can validate that the induced and climb power determinations (Equation 3 and 5) have been implemented correctly in the simulation environment. This is achieved by plotting the ratio between $(V_c + v)/v_h = (V_Z + v)/v_h$ and $V_c/v_h = V_Z/v_h$ at different forward velocities, $V_X/v_h$. The result can be seen in Figure 3 (reproduced with author's permission) where the theoretically accepted result is shown obtained from [30] and the results obtained from the simulation environment. As can be seen, the results from the simulation environment match the expected results from the theory with just some small deviations for the empirical model.

Finally, the profile drag term in Equations 2, 3 and 5 can be calculated as [29]:

$$P_{profile} = \rho A(\Omega r)^3\left(\frac{\sigma C_{D0}}{8}\right)\left(1 + 3\mu^3 + \frac{3}{8}\mu^4\right) \tag{7}$$

where $\Omega$ is the angular velocity of the spinning propeller, r is the rotor radius, $C_{d0}$ is the profile drag coefficient of the airfoils, $\sigma$ is the solidity representing the ratio of blade lifting area to rotor disk area and $\mu$ is the rotor advance ratio both defined as:

$$\sigma = \frac{(number\ of\ blades)chord}{\pi r} \tag{8}$$

$$\mu = \frac{V_\infty cos(\alpha_{tpp})}{\Omega r} \tag{9}$$

The application of momentum theory offers the ability to estimate the power required in vertical flight using Equations 3 and 5 for VTOL-capable vehicles inside the TEM system.

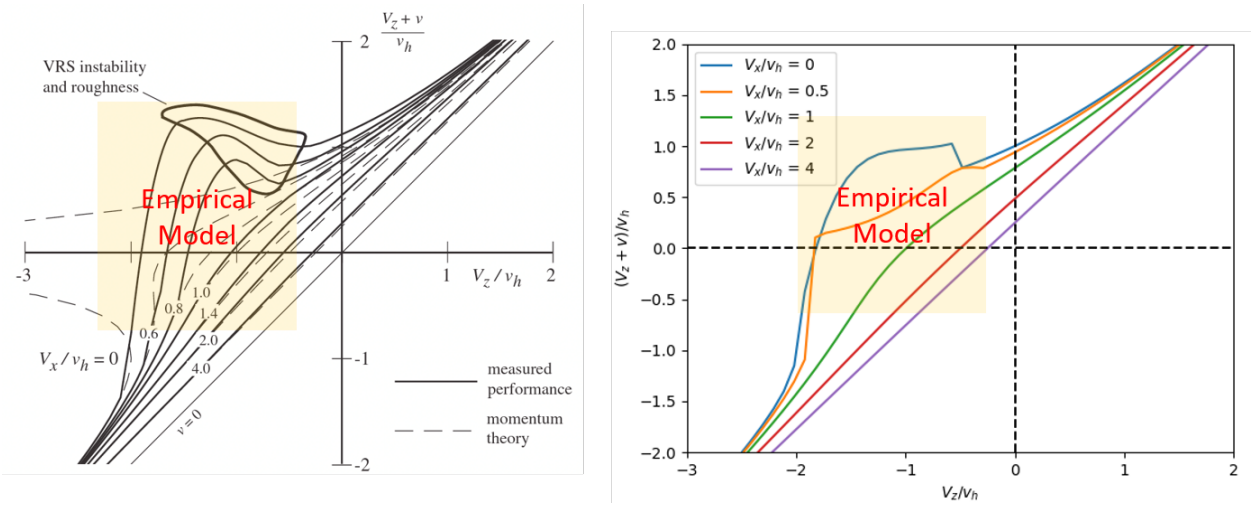


**Fig. 3 Induced and Climb Power in Forward Flight: Literature [30] (left) and Simulation (right)**

*3. Lift+Cruise Transition*

The presented approach for power requirements in the previous section is applicable for pure VTOL flight, that is flight where lift is solely generated by vertical rotors. However, lift+cruise vehicles generate lift in certain flight phases using a combination of forces generated by the wing and forces generated by vertical rotors. As a result, these equations do not accurately capture the power requirements that the powertrain module should supply to support flight. One example of a flight phase where this occurs is the transition for a lift+cruise vehicle from either lift-on-rotors to lift-on-wing or vice-versa. Additional modeling is required to accurately predict the power requirements at each instant during the transition.

Similarly as in [31], the transition between flight on vertical rotors to flight on wings and vice-versa can be modeled as a vertical and horizontal force balance. Where [31] considers the average lifting thrust over the transition in the force balance, the quadratic relation of lift with freestream velocity, $L = 1/2\rho V_\infty^2 S C_L$, can instead be used as a constraint during the transition. This is shown visually in Figure 4 in the case of a level transition, i.e. no altitude change, the sum of lift generated by the vertical rotors with the lift generated by the wing must equal the vehicle weight.

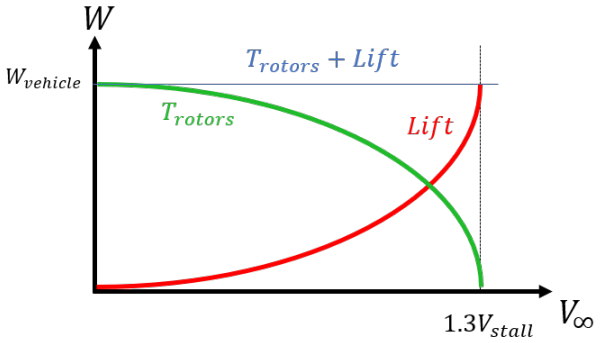


**Fig. 4 Vertical Force Balance during Level Transition**

Before modeling the transition in more detail, a few simplifying assumptions can be made. Firstly, nonlinear aerodynamic interactions between the rotor-induced downwash on the vehicle structure will be considered by using an adjustment factor on vehicle weight in vertical flight. This weighing factor accounts for the complex aerodynamic rotor/rotor, rotor/wing, and rotor/fuselage interactions that in essence cause additional losses and drag with respect to the momentum theory equations discussed in the previous section. Additionally, the vertical rotors of the lift+cruise vehicle are fixed with respect to the aircraft vertical axis such that vertical thrust ($T_Z$) is produced in the negative body z-axis while the horizontal pusher propeller is installed in-line with respect to the aircraft longitudinal axis producing

horizontal thrust ($T_X$). Horizontal and vertical accelerations ($a_X$ and $a_Z$) are modeled as constant accelerations throughout the transition, and the vertical rotors are not used to induce forward flight such that only the horizontal propeller is responsible for forward flight.

Figure 5 shows the free body diagram during a level transition, i.e. no net altitude change. Utilizing Newton's Second Law to sum forces in the Z- and X- directions provides the 2-dimensional equations of motion shown in Equations 10 and 11 where $K$ is the weighting factor to account for the complex aerodynamic interactions, $L$ is the produced wing lift, $D$ is the aerodynamic drag of the vehicle, $W$ is the weight of the vehicle and $\alpha$ is the vehicle angle of attack.

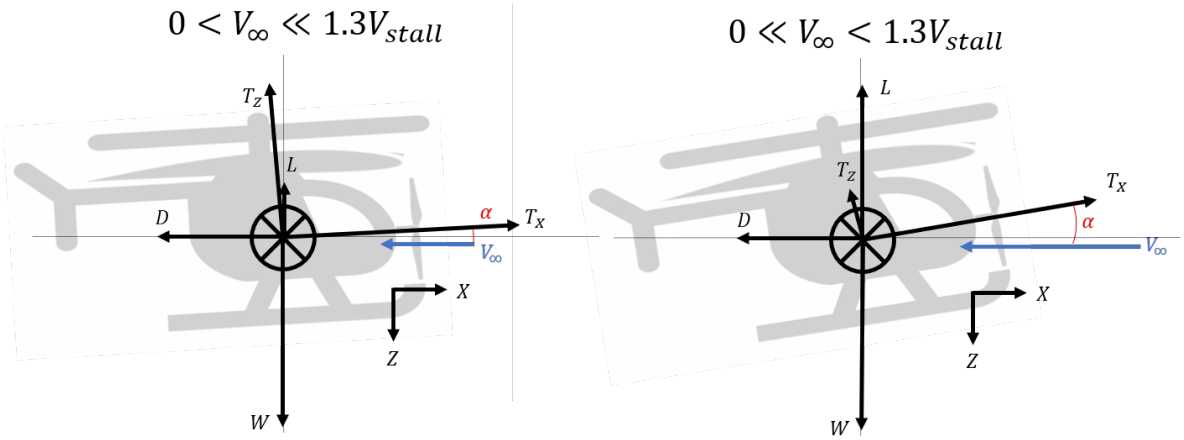


**Fig. 5 Level Transition Free Body Diagram for a Simplified Lift+Cruise Vehicle**

$$T_X \cos(\alpha) - T_Z \sin(\alpha) - D = ma_X \tag{10}$$

$$-T_X \sin(\alpha) - T_Z \cos(\alpha) - L + KW = 0 \tag{11}$$

Figure 6 shows the free body diagram for a non-level transition in which the aircraft is climbing/descending during transition resulting in an effective flight path angle $\gamma$. The equations of motion for a non-level transition can be determined as shown in Equations 12 and 13.

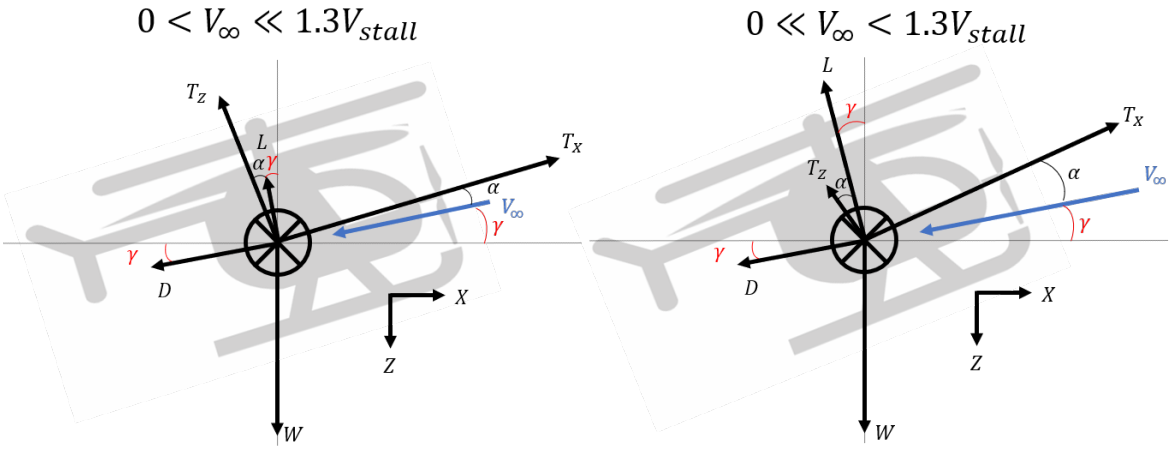


**Fig. 6 Unlevel Transition Free Body Diagram for a Simplified Lift+Cruise Vehicle**

$$T_X \cos(\gamma + \alpha) - T_Z \sin(\gamma + \alpha) - D\cos(\gamma) - L\sin(\gamma) = ma_X \tag{12}$$

$$-T_X \sin(\gamma+\alpha) - T_Z \cos(\gamma+\alpha) + D\sin(\gamma) - L\cos(\gamma) + KW = ma_Z \tag{13}$$

Equations 10-13 provide the equations of motion for a level and non-level transition respectfully. Referring to Figure 4, for a transition from hover to horizontal flight the weight carried by the vertical rotors decreases quadratically as the lift produced by the wing increases quadratically. Additionally, one of the primary assumptions is a constant acceleration during the transition which therefore establishes the velocity profile as a linear increase from hover to $1.3V_{stall}$. After consultation with industry experts on the modeling of these vehicles, the angle of attack is chosen to remain at zero for the initial 70-80% of the transition with a sharp increase towards the end of the transition to minimize the overall drag and therefore energy spent during the maneuver. A reverse procedure is scheduled for the opposite transition. The transition trimming can subsequently be defined as an optimization problem as discussed before and in [2]. Initially, the transition maneuver is discretized into various individual points. At each point, the velocity of the vehicle is known given the linear acceleration schedule. With the known vehicle freestream velocity and angle of attack, the lift, drag and thrust of the vehicle can be determined using the fixed-wing vehicle model developed in [2]. Additionally, the required horizontal and vertical thrust such that Equations 10-13 are satisfied for the desired horizontal acceleration, vertical acceleration, and flight path angle can be calculated. The vertical power required during the transition can then be determined using the known required vertical thrust by solving Equation 5. The total power required for the transition maneuver is then the sum of the horizontal power required and vertical power required:

$$P_{transition} = T_X V_\infty + P_{vertical} \tag{14}$$

An example power curve during the transition of a lift+cruise vehicle from hover to flight fully supported on the wing can be seen in Figure 7 where the sharp increase at the end of the maneuver is caused by the sharp increase of angle of attack.

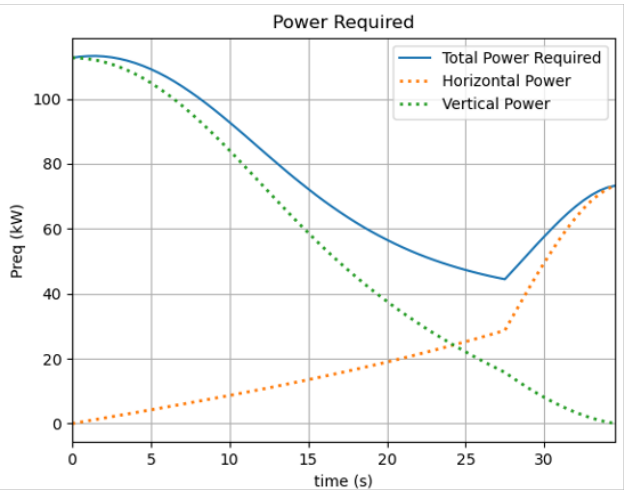


**Fig. 7 Example Transition Power Curve**

*4. Takeoff and Landing Modeling*

Flight post-takeoff and pre-landing can be modeled using the trim algorithm for cruise, climb, descend and turn conditions as shown in [25][2]. Slightly modified versions of these various flight phases concatenated with each other can be used to produce the on-wing and vertical takeoff and landing maneuvers. The on-wing takeoff for the vehicle is modeled as an acceleration from standstill up to $1.3V_{stall}$ after which a climb is initiated at the vehicle specific best climb angle up to an altitude of 50 ft. Above an altitude of 50 ft the aircraft continues climbing at the vehicle's best-rate-of-climb climb rate and velocity until an altitude of 1,000 ft is reached. For power considerations, the simulated ground roll and initial climb to 50 ft is performed at the vehicle's Maximum Takeoff Power (MTOP) setting while the climb from 50 ft to 1,000 ft is considered to be at Maximum Continuous Power (MCP) setting. The on-wing landing maneuver follows a similar approach where the vehicle for a given descend rate will descend to the runway at a speed equal to $1.3V_{stall}$ where the power is determined using Equation 1.

The vertical takeoff is modeled using a similar approach as shown in numbered locations 1, 2 and 3 in Figure 2. The maneuver initiates with a 2 second hover to model the vertical lift off from the ground followed by a timed vertical climb at a specified climb rate. Next, another timed hover is performed followed by either a level or unlevel transition up to a velocity of $1.3V_{stall}$ and specified a climb rate. Once the transition is complete, a climb at the vehicle specified best-rate-of-climb climb rate and velocity is performed until an altitude of 1,000 ft is reached. The total power required for this maneuver is calculated using Equation 14. Finally, the vertical landing is modeled using the reverse procedure as above discussed for the vertical takeoff consisting of a descend, transition, hover, vertical descend and 2 second hover.

*5. SOC Limit Calculation for Landing and Reserve*

In order to assure the vehicle has enough remaining energy to complete the required landing at the airport or helipad, a landing can be simulated inside the TEM architecture to assure mission feasibility. Using the above approaches for on-wing and vertical landing, a minimum SOC can be found required to support the landing. Additionally, 14 CFR §91.151 provides reserve energy requirements for flight in (Visual Flight Rules) VFR conditions. This reserve mission can be modeled as a timed cruise at a set altitude. Including this feature in the TEM system provides a minimum SOC required after landing such that enough energy is left to perform a diversion maneuver.

## B. Mission Power Requirements

With the addition of the vertical flight power determination described in the previous sections, a typical mission of a VTOL-capable lift+cruise vehicle can now be modelled (Figure 8). For vertical takeoff, hover, and vertical descent, Equations 3 and 5 can be used to estimate the power required for these flight phases. Using the approach discussed in the previous section, the required power for a transition maneuver can be found while for all other fixed-wing operations Equation 1 can be used. The powertrain module can now subsequently take these mission power requirements to analyze battery health, battery charge, and other power related metrics.

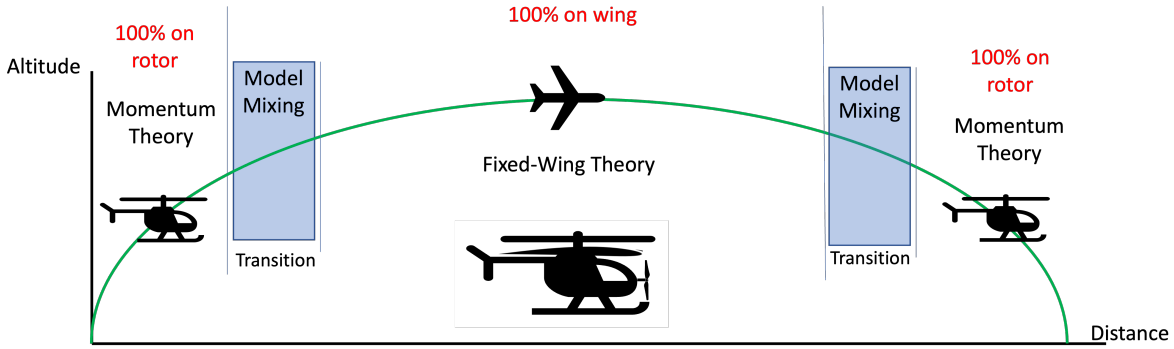


**Fig. 8 Lift+Cruise Vehicle Mission Modeling**

## C. Powertrain Modeling

The electric powertrain must be modeled in order to quantify the energy drawn from the vehicle battery in relation to the mission power requirements provided. Using inputs from the flight dynamics code, individual component models are assembled into an overall powertrain framework, where fundamental electrical parameters such as battery voltage and current can be simulated. Utilizing individual component models also allows for individual component temperatures to be tracked over a wide range of operational conditions in order to assess how temperature restrictions impact the operation. Validation and testing of the powertrain models can be performed with the same flight test data and surrogate models presented in [2]. However, the surrogate models presented in this earlier work are not so easily scaled to new concepts like the VTOL-capable lift+cruise concepts discussed in this paper, for which little or no flight test data is available. To develop a more flexible model, the modular component-level modeling framework from the previous work was modified; replacing the battery, motor/inverter, and thermal models with simple first-order physics-based models and calibrated using the surrogate models previously validated with real-world flight test data. The appropriate components specific to a configuration can then be defined in parallel; for a lift+cruise configuration this comprises the

separate motors and inverters of the vertical and horizontal thrust systems, which both draw power from the shared battery. By modeling these subsystems in parallel, the power requirements, thermal load, and subsequent component temperatures are obtained for each, allowing both subsystems to influence the trajectory generation algorithm.

*1. Key Metrics*

Characterizing the energy state of a non-linear system like a lithium-ion battery pack requires several parameters. The output of the physics-based battery model provides a line voltage and current required for the input mission power, and from an electrical standpoint, the product of these defines the total power required from the battery at a given time. These metrics, along with the individual temperatures of the battery, motor(s), and inverter(s) are tracked to assess key aspects of the state of the powertrain.

To provide a more high-level assessment of the energy state of the aircraft over the course of the mission, State-of-Charge (hereafter referred to as SOC) is estimated from the battery outputs. This provides a ratio of the current charge available to the total capacity (integrated current), here given as a percentage. The maximum capacity of any given battery is itself variable, and the relative health of a battery to its original state when new is conventionally assessed with the State-of-Health metric (hereafter referred to as SOH), given in this paper as a percentage.

Given this consideration, the actual energy available to the aircraft at a given instant is computed by the multiplication of the battery voltage and the total charge remaining. Throughout the mission, changing power requirements cause the battery voltage to fluctuate, with a higher current demand resulting in a greater voltage drop. This corresponds to a lower available energy at high power settings, and perhaps more dangerously, a higher available energy at lower power settings. In this latter case, a subsequent increase in power setting (particularly at low energy) may cause an unexpected drop in available energy, an issue not experienced by the pilots of conventionally powered aircraft. This necessitates of an integrated metric such as SOC to analyze useful remaining range and endurance. Even then, the non-linear dynamics of lithium-polymer battery cells means that performance deteriorates as SOC approaches zero; a result of the rapidly increasing internal resistance causing a lower power output. Although not a primary concern throughout most of a mission, this becomes critical for landings at a low SOC, especially if a vertical landing is to be attempted. This is tracked by determining the required current to cause the battery voltage to drop to the minimum allowable voltage, and therefore the maximum power that can be attained before reaching the minimum voltage.

*2. Battery Model*

A Thevenin equivalent circuit model models the lithium-polymer battery and allows a scalable model that can apply to the small conventional Velis Electro, as well as the larger NASA RVLT vehicle. Equivalent Circuit Modeling (ECM) is a model-based state of charge estimation method that approximates the battery as an equivalent electrical circuit. Equivalent circuit components are characterized by experimental measurements as a function of SOC & temperature. Parameterization data from the NASA X-57 electric demonstrator aircraft [12] is used for this characterization, and models cell very similar to that used in the Velis Electro. Thevenin voltage (Uth) and state of charge (S) are governed by the following differential equations:

$$\dot{U_{Th}} = \frac{-U_{Th}}{R_{Th}C_{Th}} + \frac{I_L}{C_{Th}} \tag{15}$$

$$\dot{S} = -\frac{I_L}{Q_{max}} \tag{16}$$

In order to define the battery pack of the RVLT Lift+Cruise vehicle, the generic 18650 cell-based battery model used for modeling the aforementioned notional Velis Electro (which was in turn adapted from the X-57 Maxwell equivalent circuit battery model [13]) can be appropriately to meet the power demands of a specific configuration. It is acknowledged that the current state of battery technology may limit the feasibility of a conceptual models such as those from the RVLT program, and so improved battery specific energy density can be simulated by modeling additional battery packs added with no added weight penalty. Integration of the battery model over discrete time-steps throughout the mission then provides a range of overall powertrain metrics that can be used to inform trajectory generation; SOC and component temperatures being two primary examples.

*3. Motor/Inverter Model*

In the case of the conventional Velis Electro, the combined E-811 AC induction motor and H300A inverter form the Electric Propulsion Unit (EPU). An efficiency map provided by the manufacturer allows interpolation of the varying EPU efficiency throughout a mission (as a function of requested torque and RPM). In the case of the notional lift + cruise configuration, the performance of the conventional Velis motor has been scaled to form the cruise motor, based on the assumption of a similar type AC induction motor/inverter pairing. In the absence of real-world efficiency data for the extremely powerful motors needed to power the RVLT (not yet technically viable), an efficiency similar to current commercial electric aircraft motors has been assumed. In the case of this paper, the notional Velis Electro motor model - previously validated with flight test data made available by the manufacturer - was used as the baseline model for the RVLT motor cruise motor efficency. For the lift motors that are required to operate for only a small segment of the mission, and at a relatively fixed RPM, a fixed efficiency value of 0.85 is used. This value also reflects the inefficiencies particular of the vertical lift subsystem of the powertrain, which is expected to operate at or near the maximum rated continuous power of the components.

*4. Thermal Modeling*

As demonstrated by Falck et al, when thermal constraints are considered - particularly in climb - there is a significant impact on the resulting optimal trajectory [13]. Therefore it was considered vital to independently model the temperature of the battery, motor, and inverter, allowing the impact of each to be independently quantified. As cooling systems can vary significantly between aircraft, a simple yet robust model was required to gauge the impact of thermal constraints, that could be calibrated for different configurations. As can be seen below, first-order temperature models were developed, taking as an input the thermal power calculated using I2R heating, with current and resistance obtained from the battery equivalent circuit model. It is assumed this is dissipated heat energy, removed via the cooling system, modeled in this paper with first-order convective losses. Although the individual cooling system may vary between aircraft, manufacturer-provided flight data can be used to calibrate simple models, as has been done in this paper, allowing coefficient estimates to be tuned to match the real-world response across a range of operational conditions.

$$P_{therm} = I_L^2(R_0 + R_{Th})n_{cells} \tag{17}$$

- Ptherm = thermal power (W)
- IL = cell current (A)
- R0 = internal resistance (Ω)
- RTh = Thevenin resistance (Ω)
- Ncells = number of cells

$$P_{net} = P_{therm} - hA(T_{batt} - T_{amb}) \tag{18}$$

- Pnet = net power contributing to temp rise
- h = battery heat transfer coefficient
- A = radiator area

$$\frac{dT}{dt} = \frac{P_{net}}{mC_p} \tag{19}$$

- dT/dt = rate of temperature change (C/s)
- M = battery mass
- Cp = specific heat

### D. Trajectory Generation

The primary goal of the trajectory generation and optimization is to understand and account for the energy used by electric aircraft over the course of a trajectory between a starting-point and an end-point. This requires knowledge of the aircraft's flight path since the energy used from the battery is derived from the power required by the vehicle. Therefore, a trajectory generation environment is developed to provide feasible and energy-optimized flight paths subject to the powertrain and vehicle dynamics discussed in the previous sections. The environment is developed to support electric CTOL and VTOL vehicles with the dynamics and trim conditions included. The result is a discrete set of trim conditions corresponding to physical locations along a trajectory.

As discussed, two main functionalities are envisioned for the Trajectory Energy Management (TEM) system. The first functionality focuses on generating trajectories during the pre-flight planning phases to find an energy-optimized trajectory linking departure and destination locations. The second functionality could provide pilots with real-time in-flight information about reachable airports to facilitate decision-making by flight crews during contingency situations. As part of this second use-case, the concepts of remaining energy, remaining range, and remaining endurance are explored.

*1. Environment Data*

The vehicles of interest in this research are CTOL and VTOL electrified aircraft, which often operate closer to the ground than larger commercial planes. As a result, the generation of trajectories need to consider the terrain to ensure a clearance of 1,000ft over the ground is maintained as per 14 CFR §91.119. To do so, radar elevation data from the United States Geological Survey's Shuttle Radar Topography Mission (SRTM) is leveraged and used for collision checks during simulation. The GMTED2010* dataset has a 7.5 arc second spatial resolution, or about 225 meters in our area of interest. Subsequently, the radar elevation data can be converted into a 2D and 3D terrain map projection that can be used for visualization in the TEM system (Figure 9).

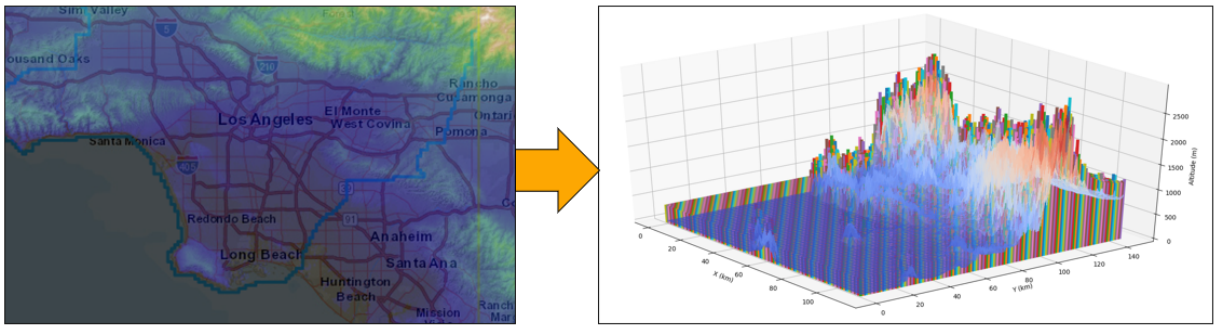


**Fig. 9 Terrain Mapping and Projection**

*2. Trajectory Formation*

The inclusion of terrain information in the trajectory generation allows for the creation of feasible flight trajectories that do not collide with terrain. By accounting for the vehicle dynamics and the powertrain models during the generation of trajectories, we can ensure that the trajectories are flyable by the vehicle. This means that the vehicle can be trimmed, enough power is always available, and no subsystem limitation is exceeded at any point along the trajectory. The vehicle dynamics and powertrain components are highly-nonlinear and complicated to model, and furthermore, there are millions of different designs. Therefore, these models must be considered 'black-box' models where data on the conditions are input and a new state is an output. This limits the ability to derive accurate steering functions within the RRT algorithm and would require lower-fidelity models in place. Rather than limiting the accuracy, a kinodynamic sampling-based planning algorithm is examined to produce feasible trajectories using a forward propagation technique, as opposed to the point-to-point connection in the steering function.

There exist techniques including kinodynamic RRT or RRT with differential constraints, which require feasibility of the edge transitions between nodes in the search tree. This may be done by solving the constrained two-point boundary value problem (TPBVP), however, this is computationally challenging. Bertsekas in [18] outlines the Minimum Principle using Calculus of Variations, a technique that requires the differential equations of the system dynamics explicitly defined. The computational and logistical requirements make this technique not suited for this area of research.

The Stable Sparse RRT (SST) algorithm, as detailed in [23] accomplishes all of these requirements while maintaining a sparse, efficient data structure. The algorithm considers the dynamics in the cost of building the tree, then forward propagates the dynamics to sample a new feasible point. The propagation methods can be done using the controls of the vehicle or at a higher level using the trimmed flight conditions. Therefore, the SST algorithm is used for further trajectory generation analysis.

*https://www.usgs.gov/coastal-changes-and-impacts/gmted2010

*3. Stable Sparse-RRT*

The propagation-based, Stable Sparse-RRT (SST) is a sampling based trajectory generation method that utilizes inherent best first selection and pruning functions to select nodes to progress from [23]. Utilizing these functions will promote relatively fast converging while leveraging near-optimal solutions. The SST algorithm is demonstrated for VTOL aircraft in the work by Nurimbetov [32] where the vehicle plans a flight path by taking off vertically, transitioning to fixed-wing flight, and planning a series of maneuvers to the goal location. A similar logic is used in this work, while minimizing the constraints that require a vertical takeoff and landing, since the vehicles of interest are often capable of both. The algorithm's derivation, proof, and steps are found in the work by Li et al [23] and pseudo code is provided in Algorithm 1.

**Algorithm 1:** Stable-Sparse-RRT(X, U, $x_0$, $T_{prop}$, N, $\Delta_{BN}$, $\Delta_S$)

**Data:** $x_0 \in X,\ N > 0,\ \Delta_{BN} + 2\Delta_S \geq \Delta$
**Result:** $p^* = \{t_1, x_1 | ... | t_f, x_f\} \in \mathcal{P}$
$cost(p^*) \leq cost(p_i)\ \forall\ p_i \in \mathcal{P}$ ;
$V_{active} \leftarrow x_0,\ V_{inactive} \leftarrow \{\}$ ;
$E \leftarrow \{\},\ G = \{V_{active} \bigcup V_{inactive}, E\}$;
$w_0.x \leftarrow x_0$ , $w_0.p = x_0$ , $W \leftarrow \{w_0\}$ ;
**for** $N$ **do**
  $x_{selected} \leftarrow BestFirstSelection(X, V_{active}, \Delta_{BN})$ ; /* Node Selection */
  $x_{new} \leftarrow MonteCarloProp(x_{selected}, U, T_{prop})$ ; /* Node Dynamic Propagation */
  *continue* ; /* Collision, Feasibility, Neighborhood Checks */
  **if** $CollisionFree(x_{selected}, x_{new})$ **then**
    **if** $LocallyBestNode(x_{new}, W, \Delta_S)$ **then**
      $V_{active} \leftarrow V_{active} \bigcup \{x_{new}\}$ ;
      $E \leftarrow E \bigcup \{x_{selected}, x_{new}\}$;
      $PruneDominatedNodes(x_{new}, V, E)$ ; /* Node Removal */
    **end**
  **end**
**end**

Figure 10 shows a simple example highlighting the processes of the Stable Sparse-RRT algorithm. The algorithm will attempt to generate a path from start to goal while avoiding obstacles. During the exploration, generated nodes can be in two main states; active or deleted as shown in Figure 10. Active nodes are feasible nodes still considered by the algorithm to propagate from, while deleted nodes have been deemed not worth exploring further by the pruning function. In order to propagate, the *best first selection* function selects nodes to become witness nodes to then analyze its surrounding for local optimal nodes. These nodes are selected to propagate from. Inactive nodes are then defined as nodes in local regions that are not the local optimum.

*4. Parameter Selection*

The list of key parameters are found in Table 1. These include the propagation time for the motion primitives, discussed in the next section, as well as the radius values, $\Delta$'s, for comparing sampled and witness nodes. The addition of the last two parameters, shrink factor and total number of SST runs, to the SST algorithm defines the asymptotically optimal algorithm: SST* [23]. At each subsequent SST run, the SST* algorithm will increase the number of runs required while shrinking the size of the search radii. This will leverage asymptotically optimal behavior of solutions with relatively fast convergence. An example of the variation in trajectory exploration from changing the values of the $\Delta$'s is shown from a top-down view in Figure 11. As can be seen, decreased values will promote more locally optimal nodes found to progress from and therefore more exploration. An important consideration from the SST theory is that the inequality must hold so that $\Delta_{BN} + 2\Delta_S \geq \Delta$ given the robust clearance, $\Delta$. This also provides assurances that $\Delta_{BN}$ balances the exploration and path quality, and $\Delta_S$ balances the sparsity and adaptability.

The $\Delta$ parameters are critical to the convergence and final path of the problem, however, other parameters can change the solution based on the dynamic constraints that are used. The propagation time must be considered in coordination with the magnitude of the $\Delta$'s as to ensure new nodes appear in the range with enough frequency. Furthermore, since a

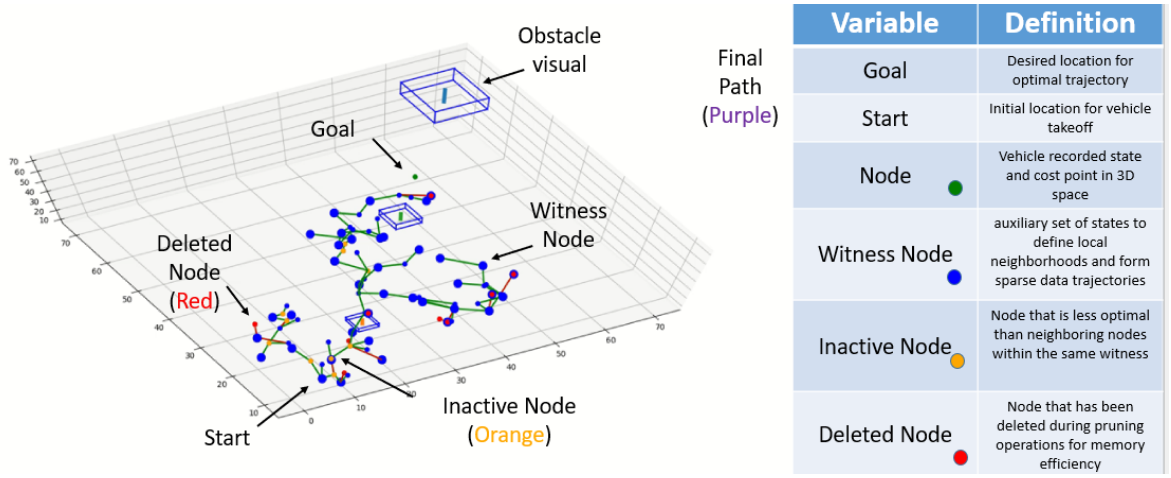


| Variable | Definition |
|---|---|
| Goal | Desired location for optimal trajectory |
| Start | Initial location for vehicle takeoff |
| Node | Vehicle recorded state and cost point in 3D space |
| Witness Node | auxiliary set of states to define local neighborhoods and form sparse data trajectories |
| Inactive Node | Node that is less optimal than neighboring nodes within the same witness |
| Deleted Node | Node that has been deleted during pruning operations for memory efficiency |

**Fig. 10 SST Example**

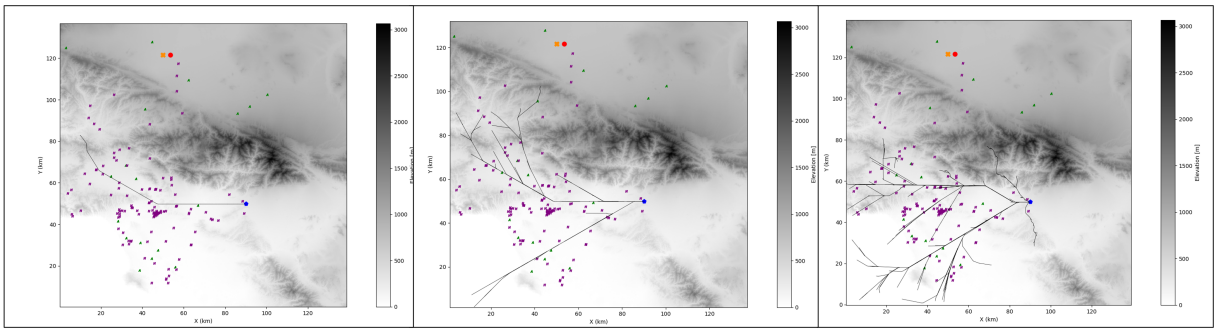

$\Delta_{bn} = 100{,}000\ (m)$, $\Delta_s = 50{,}000\ (m)$ | $\Delta_{bn} = 10{,}000\ (m)$, $\Delta_s = 5{,}000\ (m)$ | $\Delta_{bn} = 500\ (m)$, $\Delta_s = 250\ (m)$

**Fig. 11 SST $\Delta$ variable experiment**

landing maneuver must always be the final edge in the tree, the connection constraint must be defined properly so that a landing can occur at the last node. Otherwise, there will be a constraint not met, and the confidence of feasibility for the entire tree will be lost. However, if the connection constraint is too strict, any solution will take considerable time to converge. For this reason, the use of goal sampling, where the goal is selected as the propagation node with a small probability, can help in pushing the solution to the goal.

*5. Motion Primitives*

For the SST algorithm, a range of sub-functions must be defined properly for the problem of interest. A 6-DOF simulation that can handle both CTOL and VTOL vehicles must yield flyable trajectories, or trajectories along which the vehicle can be trimmed. To do so, we query the dynamics model, which going forward we will refer to as the *motion primitives* [33]. To reduce the dimensionality of the forward propagation exercise, the motion primitives are predefined trim conditions that are likely for the type of vehicle and the type of mission of interest. These include cruise, climb, descend and turn conditions, and for each of these flight phases predetermined parameters are used such as best range speed, max rate of climb speed, and standard rate turns respectively. To select the next trim condition in the forward propagation algorithm, these pre-determined trim conditions are randomly sampled using a weighted distribution to shift the distribution of trim selections based on realistic flight patterns for eVTOL vehicles. Once a trim condition is sampled, the time duration for the aircraft to fly at the trim condition is found as well through sampling from a normal distribution. This will introduce randomness in the type of trim condition as well as the duration of the segment.

**Table 1 Important Parameters for the SST Algorithm**

| Parameter | Description |
|---|---|
| Propagation Time | Maximum time for the uniform distribution that is sampled for the dynamics propagation |
| Number of Iterations | Initial number of iterations to run the SST algorithm |
| $\Delta_{bn}$ | The radius for checking for the best node near randomly sample node |
| $\Delta_s$ | The radius for checking for best node around witness nodes |
| Connect Constraint | The state constraint for connecting a node to the goal node to form a path |
| Shrink Factor | Factor for reducing the radius size |
| Total Number of SST Runs | Number of times to run SST and apply shrink factor to radii |

### E. Validation

The validation of a notional electric aircraft based on the Pipistrel Velis Electro aircraft was shown in [2]. The validation of a notional lift+cruise electric aircraft based on the NASA RVLT Lift+Cruise vehicle is performed using the NDARC output file detailing power expenditures for the design mission highlighted in Figure 2 and Figure 12. The outcome of the validation exercise is shown in Table 2 where the data was obtained from an updated NASA RVLT Lift+Cruise model originally shown in [8]. As can be seen, the simulation model accurately predicts the power requirements and energy use for the design mission. The transition from full lift on rotors to lift on wing is performed using a 10 second transition as described in section IV.A.3. The transition from wing to rotor is instead performed over a 35 second time period which explains the relatively large error in the validation result. This was decided to maintain control over the maneuver and match the desired deceleration rate. For a faster deceleration it was found that the vehicle was not able to trim successfully.

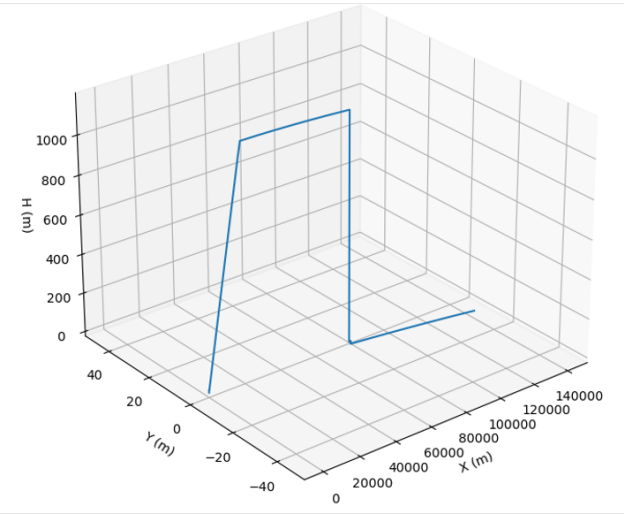


**Fig. 12 NASA RVLT Lift+Cruise Design Mission Validation**

## V. Results

The trajectory generation capability included in the TEM system can be leveraged in two modes. The first is to support pre-flight planning and the second is to support in-flight real-time re-planning. In both cases, the TEM capability is used to understand how flight crew make their decisions and to help identify the information needed by flight crew to make sound decisions. For pre-flight planning, the flight crew needs to make decisions regarding the feasibility of trajectories between an origin and a destination. The TEM system supports decision-making in this case by obtaining, simulating and analyzing potential trajectories and by simulating the evolution of metrics used by flight crews to make their decision. Subsequently, sensitivity studies of the various operational parameters used to make that decision (SOC, SOH, OAT, component temperatures) can be performed to highlight their criticality for sound decision making. For

**Table 2 NASA RVLT Lift+Cruise Vehicle Power Validation**

| Segment | NDARC Mission (kWh) | Simulation (kWh) |
|---|---|---|
| Vertical Takeoff | 11 | 11 |
| Transition (10 sec) | 4 | 4 |
| Climb | 56 | 57 |
| Cruise | 92 | 92 |
| Transition (35 sec) | 4 | 9 |
| Hover | 11 | 11 |
| Vertical Landing | 11 | 11 |
| Reserve | 105 | 101 |
| Mission Total | 294 | 296 |

in-flight real-time re-planning, the flight crew needs to assess the feasibility of flying revised trajectories and decide whether to continue to the intended destination or divert to a nearby vertiport or runway. The TEM system is used again to simulate the various metrics used by flight crew to make their decision.

### A. Pre-flight Planning: Flight from Orange County Airport (KSNA) to Riverside Municipal Airport (KRAL)

In this first scenario a flight crew is performing a pre-flight planning for a trip from Orange County Airport (KSNA) to Riverside Municipal Airport (KRAL) using a notional electric fixed-wing aircraft. Information about this route can be seen in Figure 13 where the VFR sectional map depiction is obtained from skyvector.com. The direct route ground distance is 27 nmi, the departure airport is at an elevation of 56 ft, and the destination airport is at an elevation of 820 ft. The routing is further complicated by a mountain range in between the two airports with a ridge around 4,000 ft and a maximum elevation figure of 4,500 ft nearby. A decision whether to fly straight across the mountainous terrain or fly a circuitous route must be made by the flight crew. Additionally, a lineup point is also highlighted in Figure 17 to indicate where the aircraft joins the traffic pattern for a straight-in approach to the active runway.

Using the SST trajectory generation capability of the TEM system for the initial conditions highlighted in Figure 13, two routes are found: one is a flight straight above the mountains, while the other one is a circuitous flight to the North to avoid mountains and fly over lower elevation terrain. The flight velocities for cruise and turn are set at the best range velocity for the Velis electro (90 kts) obtained from the Pilot Operating Handbook while the climb and descend velocities are set at the best-rate-of-climb velocity (75 kts)[34]. These two routes can be seen in Figure 14. The results show that the fixed-wing vehicle will have to climb higher for the direct route to clear the terrain than for the circuitous route. However, a higher final SOC is attained at the destination airport by flying straight over the mountain (48%) than for flying around it (36.5%) due to the longer routing of the circuitous route. For the given initial conditions, both routes are feasible as no temperature limits are exceeded and the final SOC is above the set limit at 20%.

The routes can further be analyzed by looking at component temperatures, SOC and power analysis during the flight. This information is shown for the over-the-mountain route and around-the-mountain route in Figure 15 and Figure 16 respectively. As can be seen, temperature time histories for the battery, motor and inverter do not exceed their respective limits. Furthermore, the power analysis shows that the requested powers to support the flight conditions is below limits indicating feasibility. Additionally, the final SOC values are above 20% and therefore both routes can be flown with the set initial conditions as shown in Figure13.

Additionally, Figure 15 and Figure 16 show predictions for remaining endurance in minutes and remaining range in nautical miles based on the average power used during the previous 5 minutes of flight. These two metrics can be useful to the flight crew to gauge whether a diversion might be necessary based on energy remaining. The plot also highlights reserve requirements which stand at 30 minutes for daytime VFR and 45 minutes for nighttime VFR as prescribed in 14 CFR §91.151. As can be seen, the VFR daytime reserve of 30 minutes is rarely met during both mission while the nighttime reserve is never satisfied indicating that the aircraft would not be able to complete the mission while meeting regulatory requirements.

Figure 15 and Figure 16 show that both the instantaneous endurance and range parameters fluctuate quite significantly throughout the flight. For example after 12 minutes of flight in the over-the-mountain use-case, the remaining flight time

is shown to the pilot as 20 minutes. After an additional 2 minutes of flight this estimation is shown at almost 35 minutes remaining flight time. This significant fluctuation might confuse a flight crew in gauging how much flight time is really remaining. Hence, unlike for traditional fossil fuel burning aircraft where the remaining flight time estimation is well understood, more understanding and research is required in order to communicate these parameters better to a flight crew.

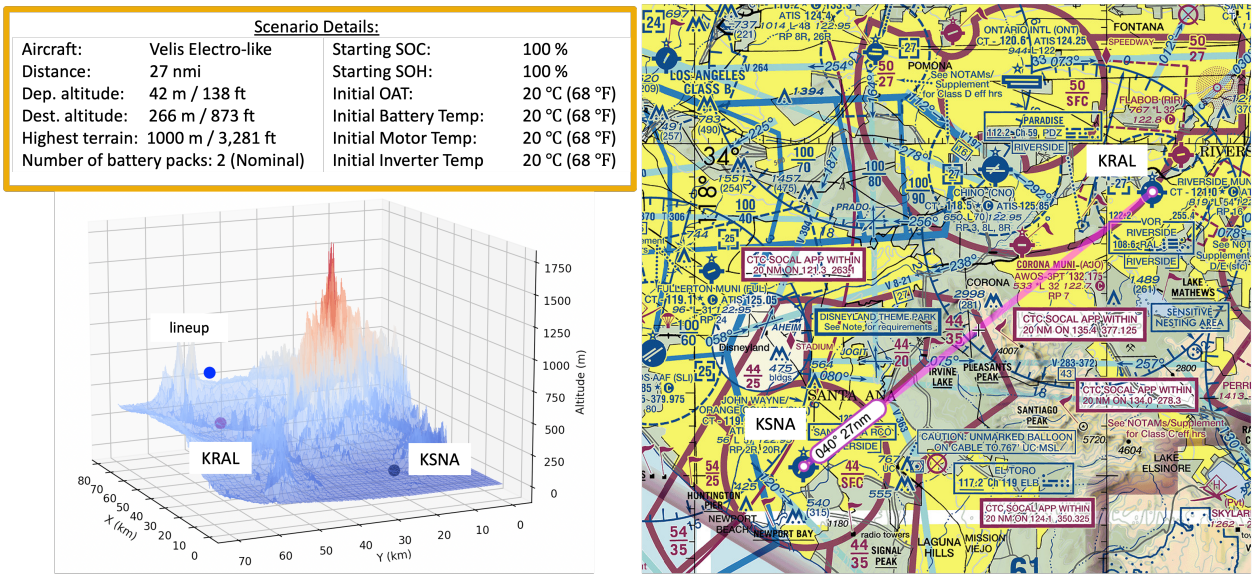


**Fig. 13 Pre-Flight Planning TEM System Use Case from KSNA to KRAL Conditions**

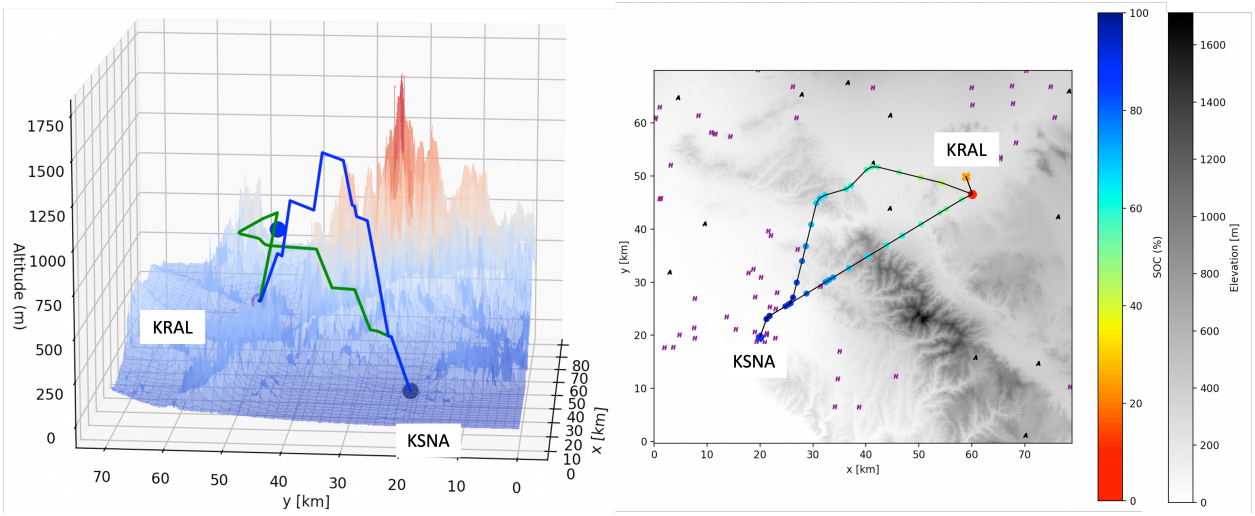


**Fig. 14 Over- and Around-the-Mountain (Blue and Green) from KSNA to KRAL**

Although the two proposed routes are shown to be feasible for the initial conditions described in Figure13, one might ask whether these two routes remain feasible when the initial conditions change i.e. a higher outside air temperature (OAT), changing component temperatures or a different initial state of charge. A sensitivity analysis is performed using a combination of these initial conditions (Table 3) and six scenarios are considered. The 'Cold Start, Standard OAT' models the nominal mission as discussed above. Then, the 'Hot Start, Standard OAT'-case models the case when the aircraft has arrived at an airport and has recharged but the powertrain component temperatures are still elevated from the previous flight. The 'Cold Start, High OAT'-case models the scenario in which the aircraft was stored indoors or in a climate controlled environment after which it is to be flown in the middle of a hot California day. To complete the set,

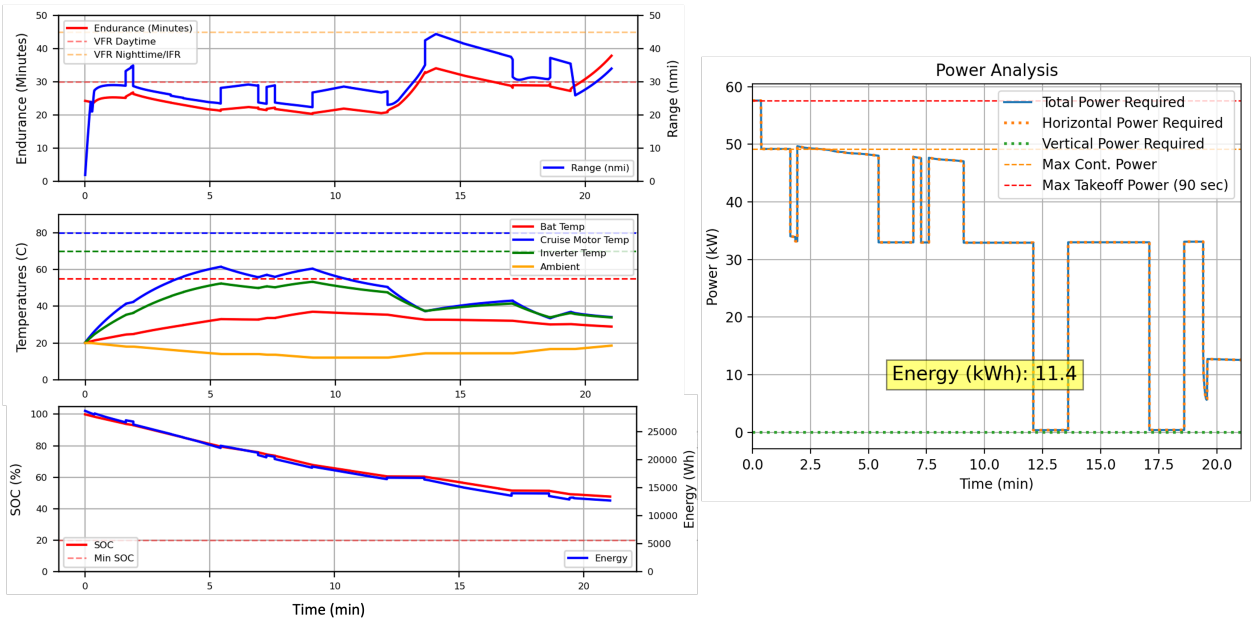


**Fig. 15 Over-the-Mountain Instantaneous Endurance and Range, SOC, Energy, Temperatures and Power Analysis**

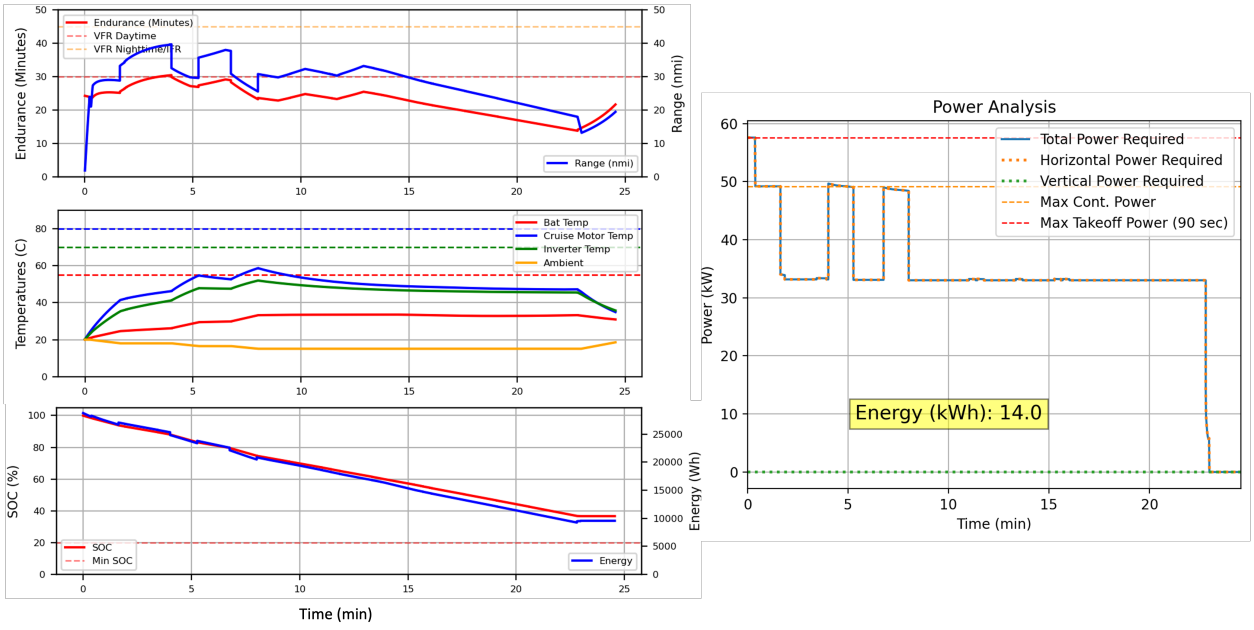


**Fig. 16 Around-the-Mountain Instantaneous Endurance and Range, SOC, Energy, Temperatures and Power Analysis**

the 'Hot Start, High OAT'-case models the aircraft flown on a hot day after recharging from a previous flight from which the powertrain components are still hot. The final two cases considered are for a lower initial SOC at 80% and a lower initial SOH at 80% which would indicate an aged battery that has gone through multiple charging cycles. The impact of these initial conditions on the evolution of powertrain component temperatures and SOC can be seen in Figure 17 and Figure 18 for the over-the-mountain and around-the-mountain use-cases respectively. Additionally, the SOC time history plot shows the set SOC limit of 20% and the required SOC to perform the landing and obtain a final SOC above

the limit of 20%. No reserve mission is considered in this use-case.

Both missions are feasible for the 'Cold Start, Standard OAT'-scenario. The 'Hot Start, Standard OAT'-scenario shows that both routes remain feasible. No visible differences can be seen in the SOC time history as compared to the nominal case. For the 'Cold Start, High OAT'-case, the over-the-mountain flight becomes infeasible due to the inverter exceeding its temperature limit. Again, no visible changes for the SOC evolution are visible. The around-the-mountain flight is the only option for the flight-crew at this point. Finally, for the 'Hot Start, High OAT'-scenario, both routes become infeasible for the aircraft.

When decreasing the initial SOC from 100% to 80% as shown for the '80% SOC'-case, the around-the-mountain trajectory becomes infeasible since the final SOC ends up being below the set limit of 20%. Additionally, although the initial SOC is decreased by 20%, the final SOC is decreased from 48% for the over-the-mountain case nominal to 25% highlighting the non-linearity of the powertrain model. Finally, if the aircraft is equipped with an aged battery for which the SOH is 80%, the over-the-mountain use case is the only feasible route since the SOC drops below 20% for the around-the-mountain case due to the more rapid discharge of the battery.

**Table 3 Considered Scenario Initial Conditions**

| Parameter | Cold Start, Standard OAT | Hot Start, Standard OAT | Cold Start, High OAT | Hot Start, High OAT | 80% SOC | 80% SOH |
|---|---|---|---|---|---|---|
| Starting SOC (%) | 100 | 100 | 100 | 100 | 80 | 100 |
| Starting SOH (%) | 100 | 100 | 100 | 100 | 100 | 80 |
| Initial OAT (°C) | 20 | 20 | 40 | 40 | 20 | 20 |
| Initial Battery Temp (°C) | 20 | 40 | 20 | 40 | 20 | 20 |
| Initial Motor Temp (°C) | 20 | 60 | 20 | 60 | 20 | 20 |
| Initial Invert Temp (°C) | 20 | 60 | 20 | 60 | 20 | 20 |

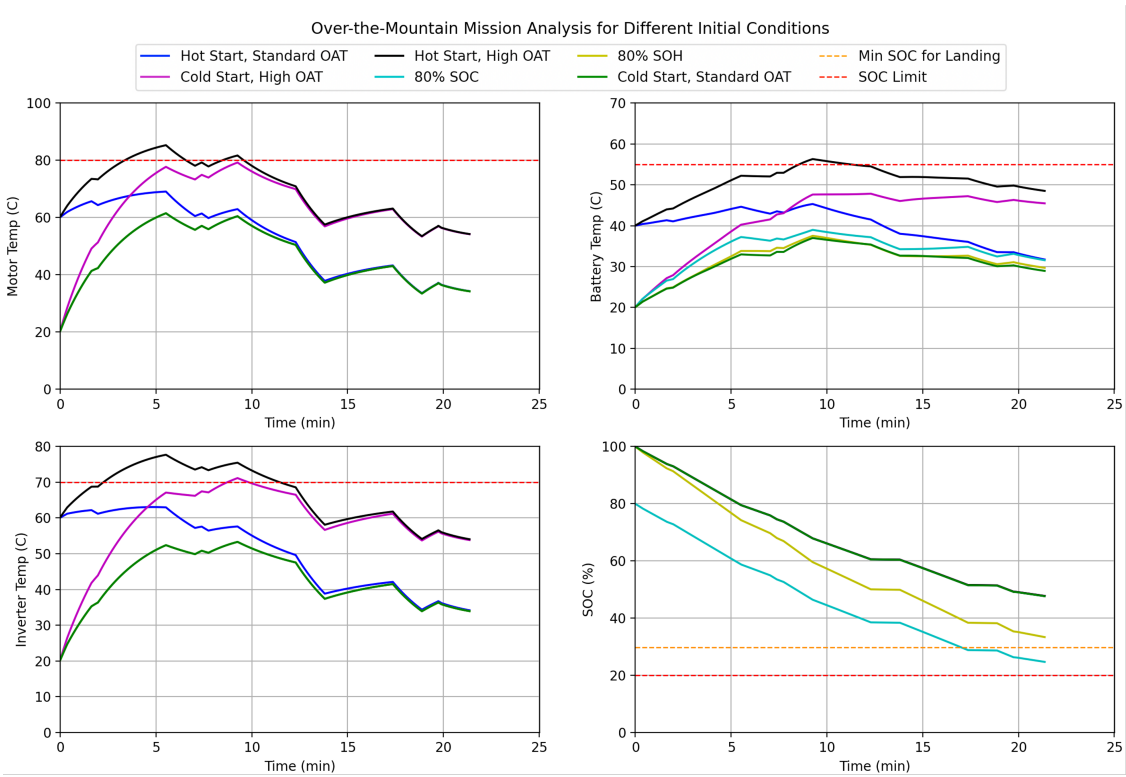


**Fig. 17 Over-the-Mountain from KSNA to KRAL Sensitivity Study to Temperatures, SOC and SOH**

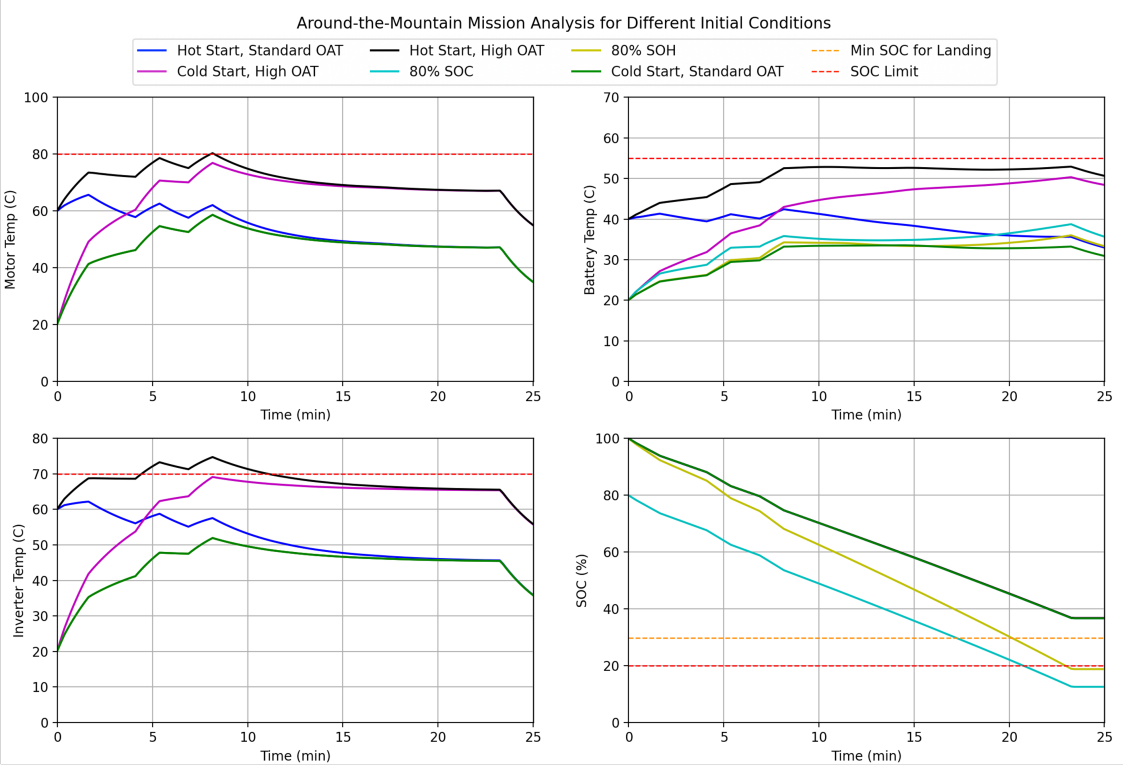


**Fig. 18 Around-the-Mountain from KSNA to KRAL Sensitivity Study to Temperatures, SOC and SOH**

### B. In-Flight Diversion Decision-Making

The previous use-case highlights the TEM system to support pre-flight planning activities. The following use-case demonstrate the use of the TEM to support in-flight replanning.

The NASA RVLT Lift+cruise vehicle is simulated to be in cruise at an altitude of 1,344m above sea level in the Mojave Desert at an initial SOC of 55% (19). Due to unexpected headwinds, the flight crew is unsure whether this is sufficient to reach the intended destination with sufficient reserves and a final SOC no less than 20%. A decision needs to be made by the flight crew to divert due to the low state of energy and to select an alternate vertiport located at California City Municipal Airport (L71), 8.4 nmi away. The assumption is that only a vertical landing is possible at this vertiport. Additionally, another alternate airport is available 17.2 nmi away where on-wing landings are assumed to be possible at the Mojave Air and Space Port (KMHV). At this point the flight crew needs to choose between a vertical landing at the nearest airport or an on-wing landing further away. The TEM system is leveraged to assess the energy requirements for these two options.

The flight velocities for cruise and descend are set at the velocities for climb and cruise as shown in Figure 2. Trajectory generation solutions for both options can be seen in Figure 20 where the final SOC for the vertical landing at L71 is 33.0% and the final SOC for the on-wing landing at KMHV is 44.5%. Both options are therefore feasible with the on-wing landing option at KMHV resulting in the higher final SOC.

The previous results show that although at a further ground distance, the on-wing landing option would result in a higher final SOC as compared to the vertical landing option. The flight crew could therefore be advised to perform the on-wing landing option in a low remaining energy scenario. Subsequently, a sensitivity study can be performed to determine under which conditions the vertical landing option would be the better option. One sensitivity that can be evaluated is the distance between the aircraft and the on-wing landing location KMHV. By arbitrarily moving the KMHV airport further while keeping the altitude at which the airport is located constant, the switch over distance can be found at which the vertical landing option at L71 becomes the more desirable option. The results of this analysis are in Table 4.

As can be seen, as the distance between the aircraft and KMHV increases, the final SOC decreases as expected. The final SOC of the battery for a vertical landing at L71 is 33.0%. Based on the sensitivity analysis, the switch over

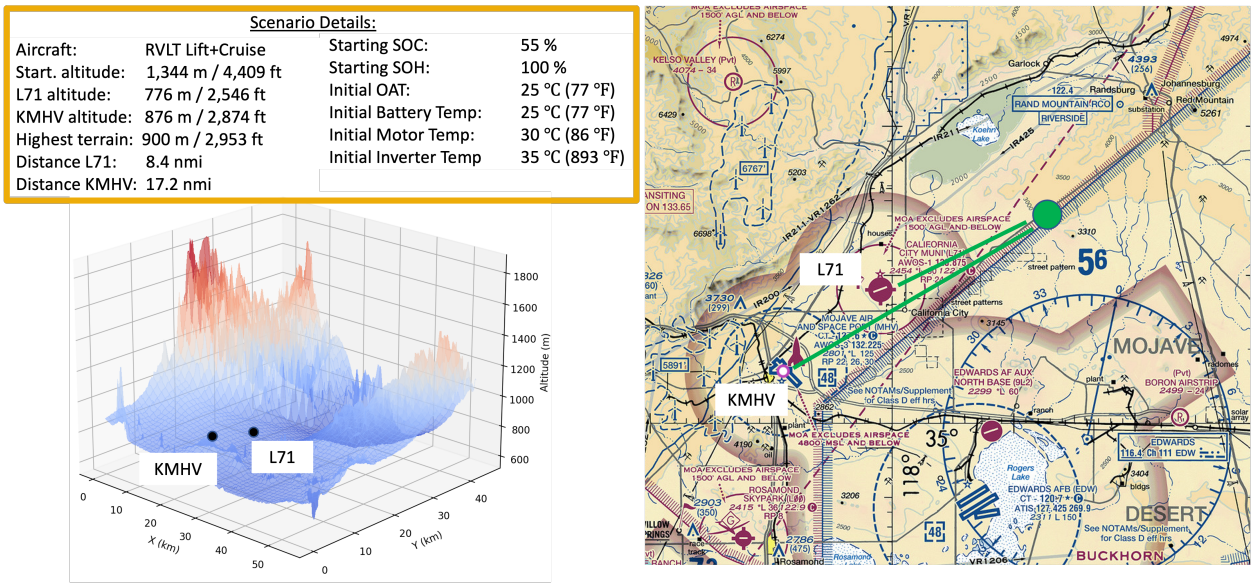


**Fig. 19 In-Flight Diversion Decision-Making Scenario**

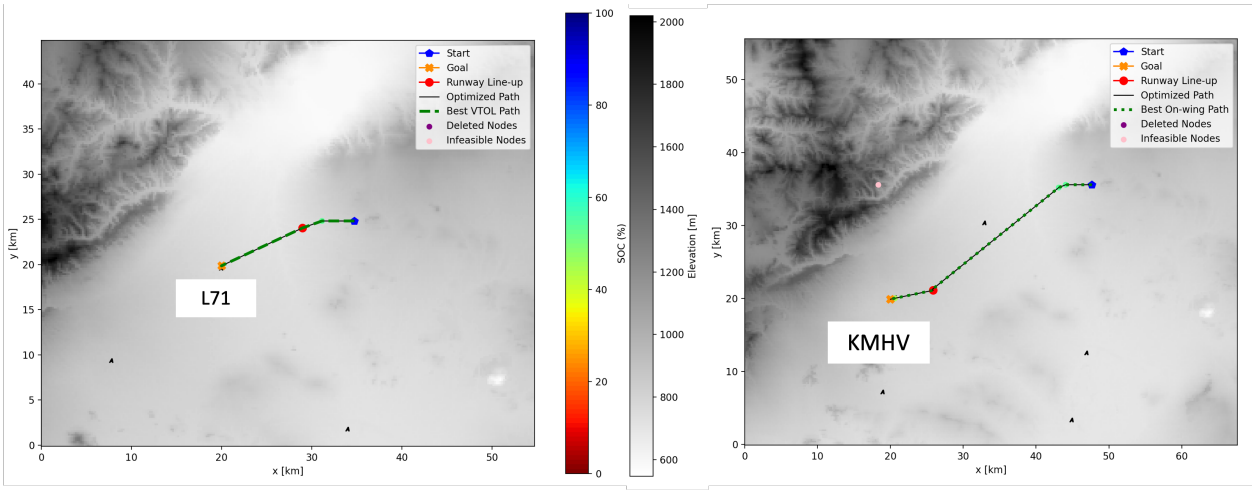


**Fig. 20 In-Flight Diversion Routes for vertical landing at L71 and on-wing landing at KMHV**

distance is 33.2 nmi. This means that for any runway closer than 33.2 nmi, the on-wing landing is the more desirable option in case of low-energy scenarios.

**Table 4 SOC Sensitivity Analysis to Distance of KMHV Airport**

| Distance (nmi) | Final SOC (%) | Distance (nmi) | Final SOC (%) |
|---|---|---|---|
| 17.2 | 44.5 | 33.2 | 33.0 |
| 18.8 | 43.5 | 34.8 | 32.0 |
| 20.4 | 42.5 | 36.4 | 31.0 |
| 22.0 | 41.0 | 38.0 | 30.0 |
| 23.6 | 40.0 | 39.7 | 29.5 |
| 25.2 | 39.0 | 41.3 | 28.5 |
| 26.8 | 38.0 | 42.9 | 27.5 |
| 28.4 | 36.5 | 44.5 | 26.5 |
| 30.0 | 35.5 | 46.1 | 25.0 |
| 31.6 | 34.5 | 47.7 | 24.0 |

# VI. Conclusion

This paper presents improvements and extensions to the TEM system presented in [2]. The vehicle simulation environment is extended to allow for the consideration and simulation of VTOL-capable aircraft. Helicopter momentum theory is utilized to obtain estimates for vertical flight power and the NASA RVLT Lift+Cruise vehicle is selected as a representative vehicle to highlight the new capabilities of the TEM system. A power validation of the vehicle model was performed to validate the implemented NASA RVLT Lift+Cruise model. Updates were presented for the trajectory generation algorithm in the form of stable sparse-RRT to produce aircraft feasible and energy near-optimal trajectories.

The updated TEM architecture was demonstrated using two-use cases; one in a pre-flight planning scenario and one in an in-flight replanning scenario. The pre-flight planning scenario demonstrated the sensitivity of key metrics such as component temperature, SOC and endurance to initial external and internal conditions such as initial component temperatures, initial SOC, initial SOH and outside air temperature on powertrain performance and overall trajectory feasibility. This further motivates the development of a Trajectory Energy Management (TEM) system that can accurately model fully-electric aircraft and powertrain behavior. The in-flight replanning scenario showed that the TEM system can be insightful to flight crews in deciding between landing locations and whether to perform on-wing or on-the-rotor landings. Future improvements will be made to the component thermal modeling and models can be developed to capture the low voltage battery and low state-of-health dynamics. Furthermore, the two main considered vehicle configurations in this study are the fixed-wing and lift+cruise. Additional variants such as vectored thrust and multicopters will be considered in future research. Additionally, current focus of this research is on fully-electric configurations, however, this will be extended to hybrid electric or hydrogen powered vehicles.

# Acknowledgments

The authors would like to acknowledge the feedback received throughout this research from Ross Schaller and Dave Sizoo.

# References

[1] Puranik, T., Jimenez, H., and Mavris, D., "Energy-based metrics for safety analysis of general aviation operations," *Journal of Aircraft*, Vol. 54, No. 6, 2017, pp. 2285–2297.

[2] Beedie, S. M., Harris, C. M., Verberne, J. A., Justin, C. Y., and Mavris, D. N., "Modeling Framework for Identification and Analysis of Key Metrics for Trajectory Energy Management of Electric Aircraft," *AIAA Aviation 2021 Forum*, 2021.

[3] Wilde, M., Kish, B., Senkans, E., Kanchwala, T., Beedie, S. M., Harris, C. M., Verberne, J. A., Justin, C. Y., and Merkt, J., "Trajectory Energy Management Systems for eVTOL Vehicles: Modeling, Simulation and Testing," *AIAA Aviation 2022 Forum*, 2022.

[4] Society, V. F., "eVTOL Aircraft Directory," , 2022. URL `https://evtol.news/aircraft`, commercial website.

[5] Bacchini, A., and Cestino, E., "Electric VTOL Configurations Comparison," *Aerospace*, Vol. 6, No. 26, 2019.

[6] Society, V. F., "Beta Technologies ALIA," , 2022. URL https://evtol.news/beta-technologies-alia/, commercial website.

[7] Society, V. F., "Wisk Aero Cora (Generation 5," , 2022. URL https://evtol.news/kitty-hawk-cora/, commercial website.

[8] Silva, C., Johnson, W., Antcliff, K. R., and Patterson, M. D., "VTOL Urban Air Mobility Concept Vehicles for Technology Development," *AIAA Aviation 2018 Forum*, 2018.

[9] Silva, C., Johnson, W., and Solis, E., "Concept Vehicles for VTOL Air Taxi Operations," *AHS Technical Meeting on Aeromechanics Design for Vertical Lift*, 2018.

[10] NASA, "Revolutionary Vertical Lift Technology Project Overview," , 2021. URL https://www.nasa.gov/aeroresearch/programs/aavp/rvlt/description/, commercial website.

[11] Patterson, M. D., German, B. J., and Moore, M. D., "Performance analysis and design of on-demand electric aircraft concepts," *12th AIAA Aviation Technology, Integration, and Operations (ATIO) Conference and 14th AIAA/ISSMO Multidisciplinary Analysis and Optimization Conference*, 2012.

[12] Chin, J. C., Schnulo, S. L., Miller, T. B., Prokopius, K., and Gray, J., "Battery Performance Modeling on Maxwell X-57," *AIAA Scitech 2019 Forum*, AIAA Aviation, American Institute of Aeronautics and Astronautics, 2019.

[13] Falck, R. D., Chin, J., Schnulo, S. L., Burt, J. M., and Gray, J. S., "Trajectory optimization of electric aircraft subject to subsystem thermal constraints," *18th AIAA/ISSMO Multidisciplinary Analysis and Optimization Conference*, 2017, p. 4002.

[14] Schnulo, S. L., Chin, J. C., Falck, R. D., Gray, J. S., Papathakis, K. V., Clarke, S., Reid, N., and Borer, N. K., "Development of a Multi-Phase Mission Planning Tool for NASA X-57 Maxwell," *Electric Aircraft Technology Symposium, AIAA*, 2018, pp. 1–14.

[15] Ayyalasomayajula, S. K., Ryabov, Y., and Nigam, N., *A Trajectory Generator for Urban Air Mobility Flights*, ???? https://doi.org/10.2514/6.2021-3013, URL https://arc.aiaa.org/doi/abs/10.2514/6.2021-3013.

[16] Wang, Z., Wei, P., and Sun, L., *Optimal Cruise, Descent, and Landing of eVTOL Vehicles for Urban Air Mobility using Convex Optimization*, ???? https://doi.org/10.2514/6.2021-0577, URL https://arc.aiaa.org/doi/abs/10.2514/6.2021-0577.

[17] Akametalu, A. K., Tomlin, C. J., and Chen, M., "Reachability-Based Forced Landing System," *Journal of Guidance, Control, and Dynamics*, Vol. 41, No. 12, 2018, pp. 2529–2542. https://doi.org/10.2514/1.G003490, URL https://doi.org/10.2514/1.G003490.

[18] Bertsekas, D. P., *Dynamic Programming and Optimal Control*, 4th ed., Vol. I, Athena Scientific, Belmont, MA, USA, 2017.

[19] Pettersson, P., and Doherty, P., "Probabilistic Roadmap Based Path Planning for an Autonomous Unmanned Helicopter," *Journal of Intelligent and Fuzzy Systems*, Vol. 17, No. 4, 2006, pp. 395–4052.

[20] LaValle, S. M., and Kuffner Jr, J. J., "Randomized kinodynamic planning," *The international journal of robotics research*, Vol. 20, No. 5, 2001, pp. 378–400.

[21] Papadopoulos, G., Kurniawati, H., and Patrikalakis, N. M., "Analysis of Asymptotically Optimal Sampling-based Motion Planning Algorithms for Lipschitz Continuous Dynamical Systems," , 2014. https://doi.org/10.48550/ARXIV.1405.2872, URL https://arxiv.org/abs/1405.2872.

[22] Kleinbort, M., Granados, E., Solovey, K., Bonalli, R., Bekris, K. E., and Halperin, D., "Refined Analysis of Asymptotically-Optimal Kinodynamic Planning in the State-Cost Space," , 2019. https://doi.org/10.48550/ARXIV.1909.05569, URL https://arxiv.org/abs/1909.05569.

[23] Li, Y., Littlefield, Z., and Bekris, K. E., "Asymptotically optimal sampling-based kinodynamic planning," *The International Journal of Robotics Research*, Vol. 35, No. 5, 2016, pp. 528–564. https://doi.org/10.1177/0278364915614386, URL https://doi.org/10.1177/0278364915614386.

[24] Nurimbetov, B., Adiyatov, O., Yeleu, S., and Varol, H. A., "Motion planning for hybrid UAVs in dense urban environments," *2017 IEEE International Conference on Advanced Intelligent Mechatronics (AIM)*, 2017, pp. 1627–1632. https://doi.org/10.1109/AIM.2017.8014251.

[25] Marco, A. D., Duke, E., and Berndt, J., "A General Solution to the Aircraft Trim Problem," *AIAA Modeling and Simulation Technologies Conference and Exhibit*, 2012. https://doi.org/10.2514/6.2007-6703, URL https://arc.aiaa.org/doi/abs/10.2514/6.2007-6703.

[26] Agency, E. U. A. S., "Type-Certificate Data Sheet No. EASA.A.573," , 2020. URL https://www.easa.europa.eu/sites/default/files/dfu/tcds_easa.a.573_is.5_0.pdf, type-Certificate Data Sheet.

[27] NASA, "NASA Design and Analysis of Rotorcraft (NDARC)," , 2022. URL https://rotorcraft.arc.nasa.gov/ndarc/, commercial website.

[28] Patterson, M. D., Antcliff, K. R., and Kohlman, L. W., "A Proposed Approach to Studying Urban Air Mobility Missions Including an Initial Exploration of Mission Requirements," *2018 Annual Forum and Technology Display*, 2018.

[29] Leishman, J. G., *Principles of Helicopter Aerodynamics*, 2nd ed., Cambridge University Press, New York, 2006, Chaps. 2,5.

[30] Johnson, W., *Rotorcraft Aeromechanics*, 1st ed., Cambridge University Press, New York, 2013, Chaps. 3,4,5,6,7.

[31] Courtin, C. B., and Hansman, R. J., "Model Development for a Comparison of VTOL and STOL Electric Aircraft Using Geometric Programming," *AIAA Aviation 2019 Forum*, 2019, p. 3477.

[32] Nurimbetov, B., Adiyatov, O., Yeleu, S., and Varol, H. A., "Motion planning for hybrid UAVs in dense urban environments," *2017 IEEE International Conference on Advanced Intelligent Mechatronics (AIM)*, 2017, pp. 1627–1632. https://doi.org/10.1109/AIM.2017.8014251.

[33] Sakcak, B., Bascetta, L., Ferretti, G., and Prandini, M., "Sampling-based optimal kinodynamic planning with motion primitives," , 2018. https://doi.org/10.48550/ARXIV.1809.02399, URL https://arxiv.org/abs/1809.02399.

[34] Pipistrel, "Pilot's Operating Handbook Velis Electro Non Type Certified," Tech. rep., Pipistrel, Slovenia, May 2021.